Utrecht University

Faculty of Science, master's programme: Experimental Physics

Master's Thesis

Non-Markovian Stochastic Resonance in a Tunable Optical Microcavity

Author:
Kevin J.H. Peters

Supervisors:
Prof. dr. Allard P. Mosk
Dr. ir. Sanli Faez
Dr. Said R.K. Rodriguez

July 30, 2019

Abstract

In this Thesis we analyze, both in theory and experiment, the phenomenon of stochastic resonance in an optical microcavity with a non-instantaneous nonlinearity. Such a non-instantaneous nonlinearity is found, for example, in media that heat and cool in finite time under constant illumination. Starting from a driven-dissipative Kerr model, we develop a new theory modeling the field in such media by introducing a memory kernel that assigns a timescale to the nonlinearity. The memory kernel makes the state of system explicitly depend on its complete history, and not only on its immediate past. The deviation from a Markovian approximation is characterized by the residence time distribution, which we find is no longer an exponential on timescales comparable to the characteristic timescale of the nonlinearity. This is an indication of level crossings which are correlated in time, a signature of non-Markovian dynamics. The model successfully reproduces experimental results demonstrating dynamical hysteresis in an optical microcavity with a thermal nonlinear medium inside.

We furthermore explore the concept of stochastic resonance in this new model. This effect manifests itself in a resonance-like peak in the signal-to-noise ratio as a function of the noise intensity. The role of the thermal relaxation time is also studied and is found to shift the peak in the signal-to-noise ratio to larger noise strengths. We finally report the first experimental observation of stochastic resonance in a thermal nonlinear medium. Comparing experimental results with simulations, we find a good agreement between theory and experiment.

Acknowledgments

Before you lies the Master's thesis entitled *Non-Markovian stochastic resonance in a tunable optical microcavity*, which was written to obtain the degree of Master of Science. It is the result of eight months of research, performed in the Interacting Photons group at AMOLF.

Initially I had some doubts before the start of the project due to the large distance I would have to travel each day. However, the project description seemed to be tailor-made for me. The complex systems master's profile, which I did prior the my graduation project, built a valuable basis in stochastics, nonlinear systems and emergent phenomena. The chance to combine the knowledge gained there with my interest in photonics really sparked my interest, and I am glad I chose to take on this project. I really enjoyed working on the topic and working at AMOLF, which is for a large part thanks to the people I got to work with.

During our first meeting, to discuss the details of the internship, Said was already able to inspire me. Because of his great enthusiasm and his eagerness to start the project, I knew I shouldn't let this opportunity pass and all initial doubts regarding the commuting went away. Although we ran into some experimental issues along the way, as happens in almost any scientific undertaking, he kept believing in the project and in me, for which I am very grateful, because in the end the struggles were completely worth the final result. Furthermore, he kept pushing me to come up with my own ideas for little side projects, which led to interesting discussions and ideas to work on. Therefore, I am glad the opportunity presented itself to continue as a PhD student afterwards. I am excited to keep on working in this very nice group for four more years to come, of which I am sure they will be packed with more challenges, but also lots of interesting physics to explore.

I furthermore want to thank Zhou Geng, a PhD student in the group, for helping me out in the lab. Prior to this project I didn't have much lab experience and my experience in optics was even nonexistent. Said ensured me this wasn't a problem; I would get the experience at AMOLF soon enough. Zhou was the one who taught me all about the different optics we use and how to use the setup itself. It was very nice working together in the lab, but our real collaboration sprang to life once the model developed in this thesis started producing its first results, reproducing Zhou's measurements. Since then we had many fruitful discussions, which helped me a lot in understanding the implications of our new model.

I would also like to express my thanks to my supervisors at Utrecht University, Allard Mosk and Sanli Faez, for their willingness to take on this task. Even though we had very few meetings during the project, it was quite clear they were also excited about this research topic. I am furthermore glad I got the opportunity to present my work to the nanophotonics people at Utrecht, both halfway the project and at the end of it.

On a more general note, I would like to thank all the people at the Center for Nanophotonics at AMOLF. The alternating weakly poster sessions and colloquia, and our monthly meetings with the Resonant Nanophotonics group were very helpful in getting familiar with each other's research and sparking new ideas. Furthermore, I am glad AMOLF has great software, mechanical and electrical engineering departments. The people working there are always happy to advise you, provide or even built components for your setup and, in general, help out where needed. Similarly, our technician, Niels, is a valuable asset of our group. Without him, we would have to spend a lot more time making and testing components for our setup, time which we can now spend on the actual research instead.

Finally, I would like to thank all family and friends for their continuous support during all my years at university. In particular my girlfriend, who has no background in physics at all, but tried her best to understand my work and, even more so, was always there for me.

Contents

Chapter 1

Introduction

The topic of stochastic processes has been around for quite some time already, with some major contributions to field in the beginning of the twentieth century regarding Brownian motion[1;2;3] and Johnson noise[4;5]. Recently, however, the topic has been gaining new momentum in the context of nonlinear systems. It may seem counterintuitive, but noise may play in fact a constructive role in nonlinear systems, when the conditions are just right. Some examples in relatively simple systems include noise-enhanced information transfer[6], signal detection[7;8] and image processing[9]. In complex networks, where spatial disorder can disrupt transfer of signals, it has been shown that transport can be assisted by the presence of noise[10], for example in neural networks[11], light-harvesting complexes[12] and in disordered[13] and ordered quantum systems[14]. Noise-assisted transport in an optical cavity network has also been observed[15] and it has been proposed to simulate complex networks found in nature, using cavity-based networks[16].

Although we ultimately aim to move our line of research to complex networks of nonlinear optical resonators to study noise assisted transport, we first need to get a thorough understanding of a single component in such a network. Even then, for the simplest nonlinear systems, e.g. double well potentials, there is rich physics to be explored. It has for example been shown that the stability of an unstable system is enhanced by a finite noise intensity[17;18]. Furthermore, the work by Kramers[19] on diffusion of a Brownian particle across a potential barrier has prompted a flurry of research. Two effects that immediately spring to mind are resonant activation[20] and stochastic resonance[21], which are related, but describe different physics. Both effects boil down to a matching of two timescales: one is the mean residence time, which is the average time spent on either side of the potential barrier, and the other is determined by a periodic modulation of the potential. Resonant activation may occur when modulating the height of the potential barrier. Cooperative interplay between the modulation and barrier crossing events causes a minimum in the mean residence time, enhancing diffusion across the barrier and increasing reaction kinetics[22;23].

The perhaps more intriguing effect of the two is stochastic resonance, where the response of a nonlinear system to a periodic signal can be optimized by the presence of a suitable amount of noise. The effect was first introduced in 1981[24] and was not much later used to explain the recurrence of the ice ages[25;26].

Although the effect is counterintuitive, the mechanism behind stochastic resonance is easy to explain in the context of an overdamped Brownian particle in a symmetric double well potential, $V(x)$, as shown in Fig. 1.1. The particle has mass m and experiences a friction or drag, leading to a dissipation rate γ. As shown by Kramers[19], the Brownian behavior of the particle causes it to randomly cross the potential barrier at the Kramers rate, which is given by

$$r_K = \frac{\omega_b \omega_t}{2\pi\gamma} \exp\left(-\frac{\Delta V}{D}\right), \tag{1.1}$$

where $\omega_b = \sqrt{V''(x_b)/m}$ is the angular frequency at the bottom of the wells, $\omega_t = \sqrt{|V''(x_t)/m|}$ the frequency at the top of the potential barrier, ΔV the height of the barrier and D the noise variance, which is the mean squared displacement for a Brownian particle.

By then periodically tilting the double well in an asymmetric fashion, i.e. applying a force on the particle, the noise will still cause the particle to transition between the two wells, even

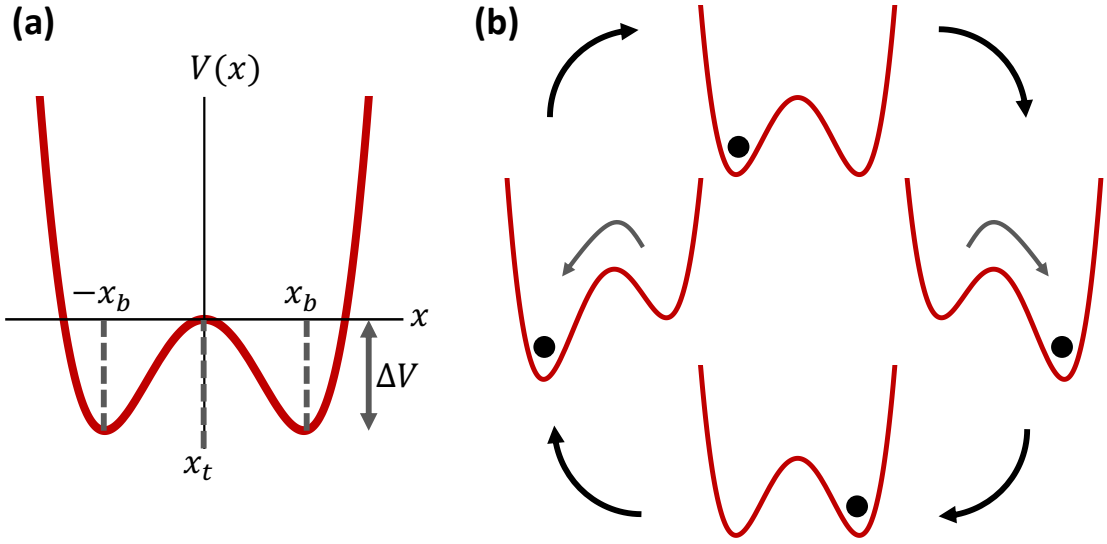

Figure 1.1: Mechanism of stochastic resonance in a double well potential. In ***(a)*** *a double well potential* $V(x) = -\frac{1}{2}x^2 + \frac{1}{4}x^4$ *is shown, with* $\pm x_b$ *the positions of the minima,* x_t *the position of the barrier maximum and* ΔV *the barrier height. In* ***(b)*** *we show the movement of a Brownian particle (black circle) in a modulated double well, demonstrating stochastic resonance: the right amount of noise synchronizes the barrier crossings with the modulation.*

while the potential barrier stays intact. It is now important to notice that the Kramers rate depends directly on the noise intensity. This means that by tuning the noise intensity, one can set the Kramers rate to satisfy the time-scale matching condition

$$\frac{1}{r_K} = 2T, \tag{1.2}$$

where T is the period of the periodic forcing on the particle. When this condition is met, the initially random barrier crossings become synchronized with the periodic forcing. In other words, the response of the system to a periodic system has an optimum, i.e. when the time-scale matching condition is satisfied. This optimum is known as stochastic resonance.

The first experimental observations of stochastic resonance in optical systems were made in a bistable ring laser in 1988 [27;28]. In these bistable ring lasers, light can travel in two directions, clockwise and counterclockwise [29]. Random switching between the two modes is initiated by spontaneous emission in the laser medium and fluctuations in the pump mechanism. Stochastic resonance in this system was demonstrated by periodically biasing the two modes, similar to the periodic forcing on a Brownian particle in a double well potential. At the nanoscale stochastic resonance was recently demonstrated in the transmission in an exciton-polariton system [30], which is bistable due to a Kerr-type nonlinearity [31]. By the same authors and using the same system, spinor stochastic resonance was observed [32], where the synchronization happens between random spin flips and a modulation in the polarization of the incoming laser. Even more recently the first observation of stochastic resonance in the quantum regime, i.e. where quantum fluctuations play the role of noise, was also reported [33]. Here the synchronization occurs between the tunneling process of electrons in a quantum dot and a periodic driving signal.

Most of these observations of stochastic resonance in optical systems at the nanoscale require extremely low temperatures. Here, however, we make use of a thermal nonlinear medium in a microcavity, as opposed to a Kerr medium. This enables us to demonstrate, to our knowledge for the first time, optical stochastic resonance at room temperature on the nanoscale.

The remainder of this Thesis is structured as follows. In Chapter 2 we provide an introduction to dissipative nonlinear optical microcavities under coherent driving, assuming the nonlinearity is instantaneous. In particular, we discuss the origin of the nonlinearity leading to effective photon-photon interactions and derive the mean field equation of motion for the field inside such cavities, largely following Ref. 34. Furthermore, we provide an assessment of the steady-states

in this mean field approximation and compare the classical bistable solutions to the unique quantum mechanical solution, which follows from the master equation for the density operator.

In Chapter 3 we introduce stochasticity into our model to study how the system behaves in a noisy environment. The addition of noise renders the previously studied bistable solutions metastable. Using simulations, we first consider a static cavity and compute the residence time statistics for both metastable states under various conditions. We use these residence times to determine the conditions for which the residence times are symmetric. We then apply a weak periodic modulation to the detuning to study stochastic resonance in a nonlinear microcavity with an instantaneous nonlinearity.

In Chapter 4 we develop a theory to model the field in a cavity when the nonlinearity is not instantaneous. This is done by introducing a memory kernel, which accounts for the timescale of the nonlinearity. The introduction of a memory kernel renders the system non-Markovian, since the future dynamics of the system now explicitly depend on its past. In the context of dynamical hysteresis, we compare simulations based on this new model to measurements and find a good agreement between theory and experiment. We then repeat the analysis provided in Chapter 3 and compare the Markovian and non-Markovian results along the way.

In Chapter 5 we move to experimental results. Starting with a description of the setup itself, we then provide a characterization of the microcavity and discuss a method to measure the thermal relaxation time of the medium inside the cavity. Finally we cover the experimental realization of stochastic resonance in an oil-filled optical microcavity at room temperature, for which the nonlinearity is not instantaneous.

Finally, in Chapter 6 we provide a summary of our most important results and an outlook to future work.

Chapter 2

Nonlinear optical resonators

In this chapter we provide a basic introduction to driven-dissipative nonlinear resonators. We will see that a change in temperature of the medium inside the cavity leads to effective photon-photon interactions, making the system nonlinear. Following the work by Drummond and Walls [34], we derive a mean field equation of motion and show that the system becomes bistable under the correct driving conditions.

2.1 Effective photon-photon interactions

When part of the laser power passing through an optical material is absorbed, the illuminated material will experience a local change in temperature [35]. Consequently, the refractive index will change, leading to nonlinear optical effects. Assuming a Gaussian laser intensity distribution, one can write the refractive index as a function of time and position (relative to the beam center) as [35;36]

$$n(\mathbf{r},t) = n_0 + \frac{\mathrm{d}n}{\mathrm{d}T}\Delta T(\mathbf{r},t), \tag{2.1}$$

where we assume an increase in temperature leads to an increase in refractive index when dn/dT is also positive. The quantity dn/dT is the thermo-optic coefficient of the material, describing the temperature dependence of the refractive index.

Note that one can write the maximum change in refractive index as (See for example Ref. 37)

$$\Delta n = \left(\frac{dn}{dT}\right)\frac{\alpha I^{(\max)} R^2}{\kappa} \tag{2.2}$$

where α is the polarisability of the medium, $I^{(\max)}$ is the laser intensity at the center of the beam, R is the beam radius and κ the thermal conductivity of the medium. Hence we can write the refractive index as

$$n = n_0 + n_2 I, \tag{2.3}$$

where $n_2 = (dn/dT)\alpha R^2/\kappa$. Therefore, the heating of the material leads effectively to the optical Kerr effect.

Note that the local change in temperature of the medium, and consequently the change in refractive index, is not instantaneous, which is what is assumed in the discussion above. The timescale associated with these changes can in fact be quite long [37], resulting in nonlinear effects which are strongly correlated in time. However, when studying dynamics on timescales much larger then the thermal relaxation time of the medium, the nonlinearity may be considered instantaneous. The implementation of a non-instantaneous nonlinearity in the model, and the consequences, will be discussed in detail in Chapter 4.

We furthermore know that the polarization of a nonlinear medium can be written as the following expansion in the electric field [37]

$$\mathbf{P} = \chi^{(1)}\mathbf{E} + \chi^{(2)}\mathbf{EE} + \chi^{(3)}\mathbf{EEE} + ..., \tag{2.4}$$

with $\chi^{(i)}$ the ith-order susceptibility, which in general is a tensor. It was shown by Bloembergen [38] that the Hamiltonian for the interaction of a single-mode field in a cavity containing such a nonlinear dispersive medium can be written as ($\hbar = 1$)

$$H = :\int \mathrm{d}^3\mathbf{r} \left\{ \frac{1}{2\mu_0}|\mathbf{B}|^2 + \mathbf{E}\left[\frac{1}{2}\left(\epsilon_0 + \chi^{(1)}\right)\mathbf{E} + \frac{1}{3}\chi^{(2)}\mathbf{E}\mathbf{E} + \frac{1}{4}\chi^{(3)}\mathbf{E}\mathbf{E}\mathbf{E}\right]\right\}:, \tag{2.5}$$

where : ... : denotes normal ordering of operators. By assuming no phase matching, second harmonic generation, and thus the $\chi^{(2)}$ term, can be neglected.

Upon making a normal-mode expansion

$$\mathbf{E} = i\left(\frac{\omega}{2\epsilon_0}\right)^{1/2}\left[\hat{a}\mathbf{u}(\mathbf{r}) - \hat{a}^\dagger\mathbf{u}^*(\mathbf{r})\right], \quad \int \mathrm{d}^3\mathbf{r}\ \mathbf{u}^*(\mathbf{r})\left[1 + \chi^{(1)}(\mathbf{r})/\epsilon_0\right]\mathbf{u}(\mathbf{r}) = 1 \tag{2.6}$$

Drummond and Walls [34] showed that the full Hamiltonian in the rotating wave approximation corresponds to a single-mode Hubbard model,

$$\hat{H}(t) = \omega_0\hat{a}^\dagger\hat{a} + \frac{U}{2}\left(\hat{a}^\dagger\hat{a} - 1\right)\hat{a}^\dagger\hat{a}, \tag{2.7}$$

where ω_0 is the fundamental cavity resonance, $\hat{a}^\dagger$ and $\hat{a}$ are respectively the creation and annihilation operators, and U now represents an effective interaction between photons.

2.2 The driven-dissipative Bose-Hubbard model

To describe a driven-dissipative cavity, we start from a second quantized single-mode Bose-Hubbard model with coherent driving, i.e. a Hamiltonian given by

$$\hat{H}(t) = \omega_0\hat{a}^\dagger\hat{a} + \frac{U}{2}\left(\hat{a}^\dagger\hat{a} - 1\right)\hat{a}^\dagger\hat{a} + i\sqrt{\kappa_1}\left(F\hat{a}^\dagger\mathrm{e}^{-i\omega t} + F^*\hat{a}\mathrm{e}^{i\omega t}\right), \tag{2.8}$$

where we denote the boson creation and annihilation operators as $\hat{a}^\dagger$ and $\hat{a}$, respectively. Here, ω_0 is the resonance frequency of the cavity, U is the effective photon-photon interaction and κ_1 is the input coupling rate of the driving field with amplitude F and frequency ω.

To account for dissipation, the system is coupled to another system, acting as a bath. For our purposes, we assume a Bose-Hubbard system coupled to a Markovian environment, in which case the dynamics are governed by a Lindblad-form master equation. The density matrix $\hat{\rho}$ therefore evolves according to

$$\frac{\partial\hat{\rho}(t)}{\partial t} = i[\hat{\rho}, \hat{H}(t)] + \frac{1}{2}\sum_l\left(2\hat{L}_l\hat{\rho}\hat{L}_l^\dagger - \hat{L}_l^\dagger\hat{L}_l\hat{\rho} - \hat{\rho}\hat{L}_l^\dagger\hat{L}_l\right) \tag{2.9}$$

Here, $\hat{L}_l$ are the Lindblad operators, which are determined by the specific coupling of the system to the environment. In our case, we consider three different localized single-particle loss channels [39]: intrinsic loss at rate γ, losses at the input at rate κ_1 and at the output at rate κ_2. The corresponding Lindblad operators [40] are $\hat{L}_1^\dagger = \sqrt{\gamma}\hat{a}$, $\hat{L}_2^\dagger = \sqrt{\kappa_1}\hat{a}$ and $\hat{L}_3^\dagger = \sqrt{\kappa_2}\hat{a}$, respectively. We thus have the master equation

$$\frac{\partial\hat{\rho}(t)}{\partial t} = i[\hat{\rho}, \hat{H}(t)] + \frac{\Gamma}{2}\left(2\hat{a}\hat{\rho}\hat{a}^\dagger - \hat{a}^\dagger\hat{a}\hat{\rho} - \hat{\rho}\hat{a}^\dagger\hat{a}\right), \tag{2.10}$$

with total dissipation rate $\Gamma = \gamma + \kappa_1 + \kappa_2$.

The mean field equation of motion can be derived (see App. A) by assuming a coherent field with amplitude $\alpha(t) = \langle\hat{a}\rangle$. This approximation is valid when the field in the cavity is strongly confined, such that the cavity modes are well-separated, and when the number of photons in the cavity is much larger than unity. Use of the master equation and the commutator $[\hat{a}, \hat{a}^\dagger] = 1$ then leads to

$$i\dot{\alpha} = \left[\omega_0 - i\frac{\Gamma}{2} + U\left(|\alpha|^2 - 1\right)\right]\alpha + i\sqrt{\kappa_1}F\mathrm{e}^{-i\omega t}, \tag{2.11}$$

where we adopted the dot notation, i.e. $\dot{\alpha} = \partial\alpha/\partial t$. Note that this result closely resembles a classical overdamped Duffing oscillator, i.e. $\ddot{x} + c_1\dot{x} + c_2 x + c_3 x^3 = c_4\cos(\omega t)$, with $c_1 \gg 1$. The main difference is that the Duffing oscillator is real valued, whereas the intracavity field we consider is complex. Albeit this difference, we may expect very similar behavior in our system.

For convenience, we move to a frame which is rotating at the driving frequency ω, such that we can write

$$i\dot{\alpha} = \left[-\Delta - i\frac{\Gamma}{2} + U\left(|\alpha|^2 - 1\right)\right]\alpha + i\sqrt{\kappa_1}F, \tag{2.12}$$

where $\Delta = \omega - \omega_0$ is the detuning.

2.3 Steady states and their stability

The steady-state field is obtained by requiring $\dot{\alpha} = 0$, i.e. it is a solution to the equation

$$0 = \left[-\Delta - i\frac{\Gamma}{2} + U\left(|\alpha|^2 - 1\right)\right]\alpha + i\sqrt{\kappa_1}F. \tag{2.13}$$

Taking $i\sqrt{\kappa_1}F$ to the left-hand side, recalling that $|\alpha|^2 = N$ is the number of photons and multiplying both sides by their complex conjugates we find that the steady-state density is given by the roots of the third order polynomial

$$\kappa_1|F|^2 = \left[-\Delta - i\frac{\Gamma}{2} + U\left(N-1\right)\right]\left[-\Delta + i\frac{\Gamma}{2} + U\left(N-1\right)\right]N. \tag{2.14}$$

Hence we can have up to three steady-state solutions.

To determine which of these solutions are stable, we use Eq. 2.12 and its complex conjugate to write

$$i\frac{\partial}{\partial t}\begin{pmatrix}\alpha\\ -\alpha^*\end{pmatrix} = \begin{pmatrix}\left[-\Delta - i\frac{\Gamma}{2} + U\left(|\alpha|^2-1\right)\right]\alpha + i\sqrt{\kappa_1}F\\ \left[-\Delta + i\frac{\Gamma}{2} + U\left(|\alpha|^2-1\right)\right]\alpha^* - i\sqrt{\kappa_1}F^*\end{pmatrix} \tag{2.15}$$

and add a small fluctuation to the steady-state field, i.e. we substitute $\alpha \to \alpha + \delta\alpha$. It is then a straightforward exercise (see App. B) to show that the fluctuations evolve according to

$$i\frac{\partial\boldsymbol{\delta\alpha}}{\partial t} = \mathbf{M}\,\boldsymbol{\delta\alpha}, \tag{2.16}$$

with $\boldsymbol{\delta\alpha} = (\delta\alpha \;\; \delta\alpha^*)^\intercal$ and the matrix $\mathbf{M}$ given by

$$\mathbf{M} = \begin{pmatrix}\left[-\Delta - i\frac{\Gamma}{2} + 2U\left(|\alpha|^2-1\right)\right]\alpha & U\alpha^2\\ U(\alpha^*)^2 & \left[-\Delta - i\frac{\Gamma}{2} - 2U\left(|\alpha|^2-1\right)\right]\alpha^*\end{pmatrix}. \tag{2.17}$$

Differential equations of this form have solutions $\boldsymbol{\delta\alpha}(t) = \boldsymbol{\eta}\exp(-i\lambda t)$, with λ the eigenvalues of the matrix $\mathbf{M}$ and $\boldsymbol{\eta}$ the eigenvectors. This implies that if for at least one eigenvalue $\mathrm{Im}(\lambda_j) \geq 0$, then fluctuations will grow in time and hence the steady-state solution is unstable. On the other hand, if $\mathrm{Im}(\lambda_j) < 0\ \forall j$, fluctuations are attenuated and hence the solution is stable.

Using the above-described procedure, we calculated the steady-state density for three different driving strengths as a function of detuning (see Fig. 2.1(a)). This shows that for small enough driving, only a single steady-state solution exists. However, for larger values of the driving amplitude, there is a detuning range for which we have three solutions, of which two are stable. The reason is purely the nonlinear term: We know that for a linear oscillator ($U = 0$) the spectral response is a Lorentzian. However, the nonlinear term can effectively be regarded as a correction to the detuning, which depends on the number of photons in the cavity. The shift with respect to the linear oscillator becomes larger when there are more photons in the cavity, which causes the Lorentzian to tilt to one side, depending on the sign of U. When the tilt is sufficient, i.e. for strong enough driving, multiple steady-state solutions arise for the same value of the detuning.

We also computed the steady-state solutions for various values of the detuning as a function of the driving amplitude (Fig. 2.1(b)). Here we see that close to resonance the number of

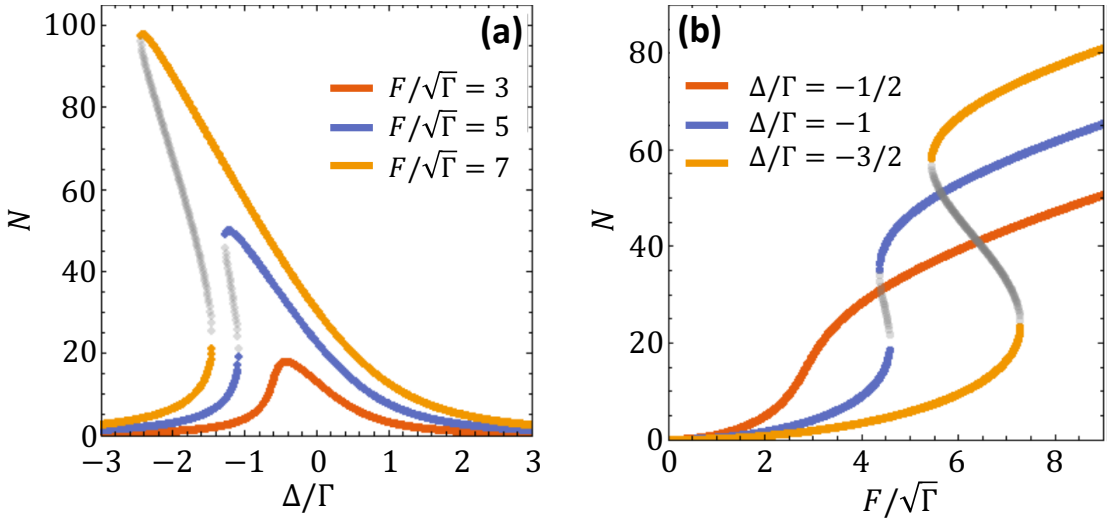

Figure 2.1: Steady-state solutions for the number of photons inside the cavity, following from the mean field description. In ***(a)*** *as a function of the detuning and in* ***(b)*** *as a function of the driving amplitude. Solid dots indicate stable solutions, whereas open circles indicate unstable solutions. Parameters:* $\Gamma = 1$, $\gamma = \Gamma/6$, $\kappa_1 = \Gamma/2$, $\kappa_2 = \Gamma/3$, $U = -\Gamma/40$.

photons increases continuously as function of the driving amplitude with only a single steady-state solution. For an increased detuning, however, an S-shape shows up, again giving rise to bistability.

For completeness we furthermore solved the master equation directly by using the methods described in Ref. 41. These solutions are shown together with the mean field solutions in Fig. 2.2. We immediately notice that the quantum mechanical steady-state solutions, i.e. the solutions of Eq. 2.10, are unique, as opposed to the mean field solutions, which show the bistability. This is due to the absence of fluctuations in the mean field description, which would make the bistable solutions metastable. In that sense the (unique) solutions following from the master equation are the weighted average of these metastable states [34;42].

Finally, since the concept of stochastic resonance is often described in terms of a double well potential, it is convenient to compute an effective potential for the number of photons in the

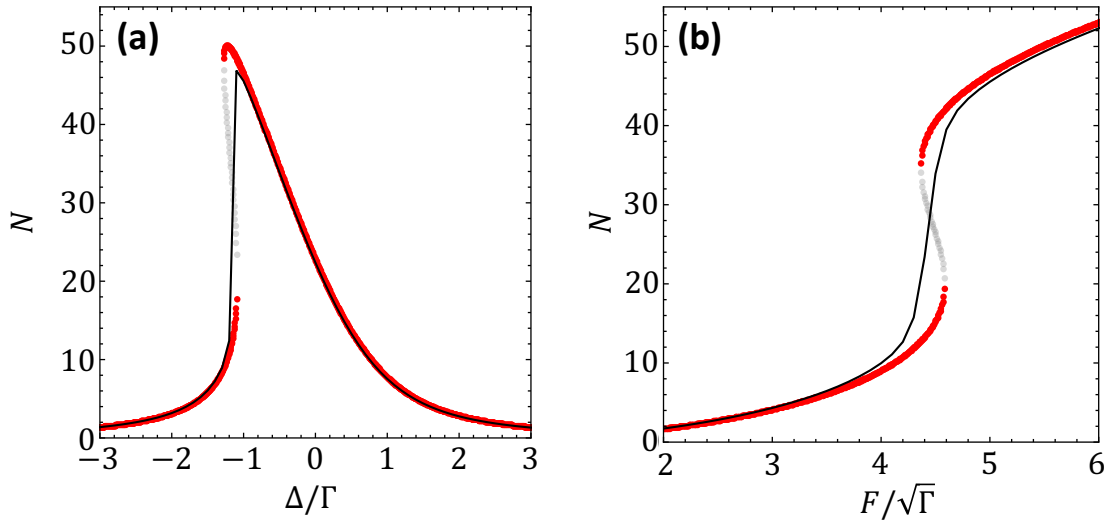

Figure 2.2: Comparison between the mean field solutions (stable in red and unstable in gray) and solutions of the quantum master equation (black). In ***(a)*** *for a fixed driving amplitude* ($F = 5\sqrt{\Gamma}$) *and in* ***(b)*** *for a fixed detuning* ($\Delta = -\Gamma$). *Parameters:* $\Gamma = 1$, $\gamma = \Gamma/6$, $\kappa_1 = \Gamma/2$, $\kappa_2 = \Gamma/3$, $U = -\Gamma/40$.

cavity to use as a reference. Following Ref. 43, we derive an effective potential $V_{\text{eff}}(N)$ from Eq. 2.14 by writing

$$\frac{dN}{dt} = \kappa_1|F|^2 - \left[-\Delta - i\frac{\Gamma}{2} + U\,(N-1)\right]\left[-\Delta + i\frac{\Gamma}{2} + U\,(N-1)\right]N = -\frac{dV_{\text{eff}}}{dN}. \tag{2.18}$$

Integration then yields

$$V_{\text{eff}}(N) = -\kappa_1 F^2 N + \frac{1}{2}\left[\left(\frac{\Gamma}{2}\right)^2 + (\Delta+U)^2\right]N^2 - \frac{2}{3}U(\Delta+U)N^3 + \frac{1}{4}U^2N^4, \tag{2.19}$$

which is a fourth order polynomial in the photon number N. Then, for a given cavity with losses κ_j and γ, and with a nonlinear medium inside giving rise to effective interactions with strength U, the shape of the potential can be controlled by changing the detuning, Δ, and driving strength, F. In Fig. 2.3 we have plotted this effective potential for three different values of the detuning and all other parameters fixed. This shows that for a set of parameters leading to bistability, we effectively have a double well potential. Moreover, by varying the detuning, we can modulate the shape of the double well, which forms the basis for stochastic resonance.

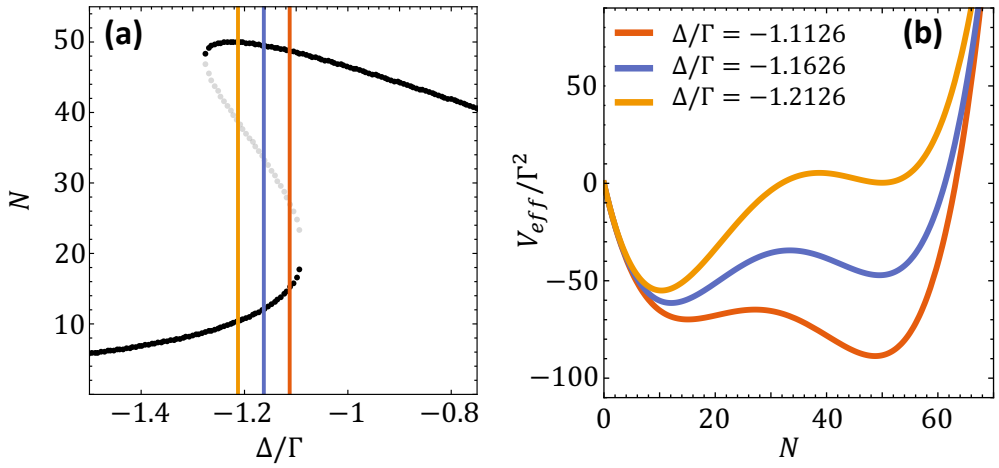

Figure 2.3: ***(a)*** *Enlargement of the steady-state solutions of Fig. 2.1(a) for $F = 5\sqrt{\Gamma}$. The colored vertical lines correspond to the values of the detuning, Δ, in* ***(b)****, where the effective potential is shown. Parameters: $\Gamma = 1$, $\gamma = \Gamma/6$, $\kappa_1 = \Gamma/2$, $\kappa_2 = \Gamma/3$, $F = 5\sqrt{\Gamma}$, $U = -\Gamma/40$.*

Chapter 3

Stochastic resonance

In this chapter we will study stochastic resonance using simulations, assuming the effective interaction U is instantaneous. In doing so, we build a basic understanding of the system under the influence of both noise and a periodic modulation of the detuning. We will then use the knowledge gained in this chapter, to apply it in the next chapter when we extend the model to incorporate an effective interaction which is no longer instantaneous.

To account for background noise and fluctuations, we include stochastic processes in our model. In general we can have noise in both the driving and the detuning, yielding a Langevin-type equation

$$i\dot{\alpha} = \left[-\Delta + D_\xi \xi(t) - i\frac{\Gamma}{2} + U\left(|\alpha|^2 - 1\right)\right]\alpha + i\sqrt{\kappa_1}F + D_\zeta \zeta(t), \tag{3.1}$$

where D_X^2 is the variance of the noise, $\xi(t)$ accounts for noise in the detuning and $\zeta(t)$ accounts both for noise in the driving field and for noise related to the dissipation. Furthermore, since the driving field can have fluctuations both in amplitude and in phase, we take $\zeta(t) = (\zeta^{(1)}(t) + i\zeta^{(2)}(t))/\sqrt{2}$, to include both in our model. Finally, we take both stochastic processes to be Gaussian with zero mean and delta-correlated[44], i.e.

$$\langle \xi(t) \rangle = \langle \zeta(t) \rangle = 0 \quad \text{and} \quad \langle \xi(t)\xi(t') \rangle = \delta(t-t'), \;\; \langle \zeta(t)\zeta(t') \rangle = \delta(t-t'), \tag{3.2}$$

Note the subtle, but important difference between the two types of noise: $\xi(t)$ is multiplied by the field α (*multiplicative noise*), whereas $\zeta(t)$ is not (*additive noise*). Hence, fluctuations due to noise in the detuning are amplified by the field α, whereas the strength of fluctuations due to driving noise is constant. In general there may exist correlations between additive and multiplicative noise[45]. In our case, however, both types of noise have a different origin and hence are uncorrelated, i.e. $\langle \xi(t)\zeta(t') \rangle = 0$.

We finally also stress another, more fundamental, difference between the noise in detuning and the one in driving. Because the noise in driving is related to the dissipation, the fluctuation-dissipation theorem[46] implies that we have a lower bound on D_ζ, given by $\sqrt{\Gamma/2}$. For the noise in detuning this is not the case.

In the rest of this chapter we will study simulations of the Langevin equation (Eq. 3.1) with only additive noise, i.e. $D_\xi = 0$, $D_\zeta = D \neq 0$. This is first done by keeping all parameters fixed to study how the system behaves under the influence of noise. Next we will apply a periodic modulation to the detuning, eventually bringing us to the notion of stochastic resonance, which will be discussed in great detail.

We hereby note that for all our simulations we will make use of the xSPDE toolbox[47] for Matlab[48].

3.1 Residence time analysis

In Fig. 3.1 we show simulations of the number of photons in the cavity as function of time for three different values of the detuning, under the influence of a moderate amount of noise

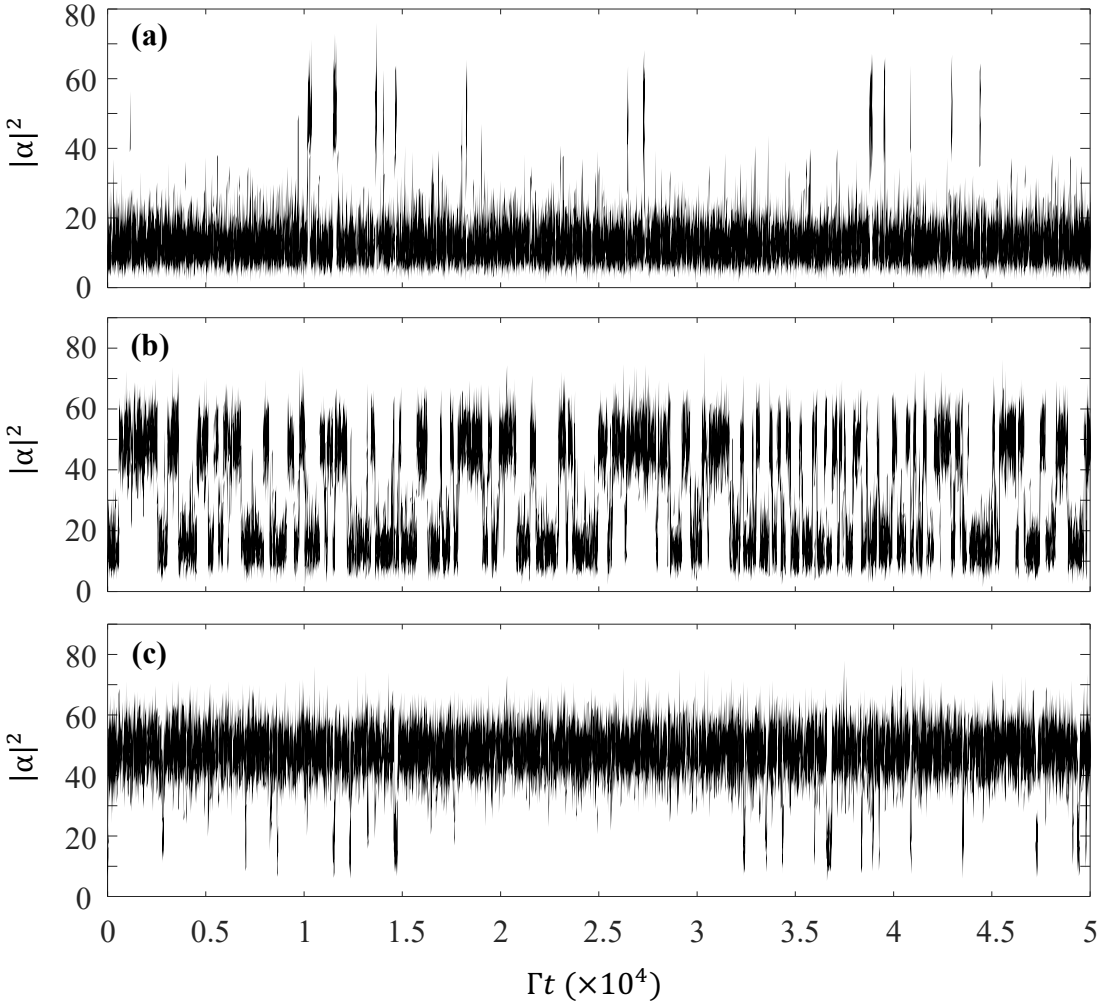

Figure 3.1: Simulation of the number of photons in the cavity as a function of time for three different values of the detuning: $\Delta/\Gamma = -1.2126$ ***(a)***, $\Delta/\Gamma = -1.1626$ ***(b)***, $\Delta/\Gamma = -1.1126$ ***(c)***. *Parameters:* $\Gamma = 1$, $\gamma = \Gamma/6$, $\kappa_1 = \Gamma/2$, $\kappa_2 = \Gamma/3$, $F = 5\sqrt{\Gamma}$, $U = -\Gamma/40$, $D = 2\Gamma$.

($D = 2\Gamma$). As can be seen in these trajectories, the noise induces switching events between the two metastable states at random intervals. Furthermore, changing the detuning allows us to set the average time the system spends in either of the two states, because the detuning determines the relative depth of the two wells (Fig. 2.3). We can therefore bias the system to a specific state as can be seen in the trajectories (see again Fig. 3.1). This is also evident in the corresponding probability distributions of the photon number shown in Fig. 3.2.

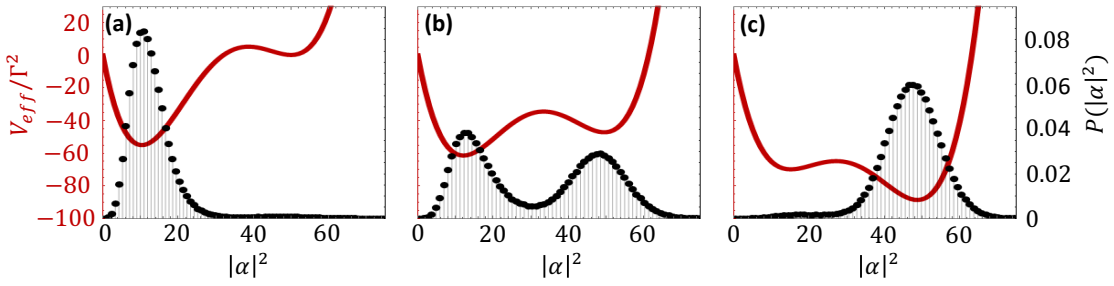

Figure 3.2: In black we show the probality distribution of the photon number $P(|\alpha|^2)$ *for three values of the detuning. The effective potential is also shown in red for reference. Simulation parameters are the same as in Fig. 3.1.*

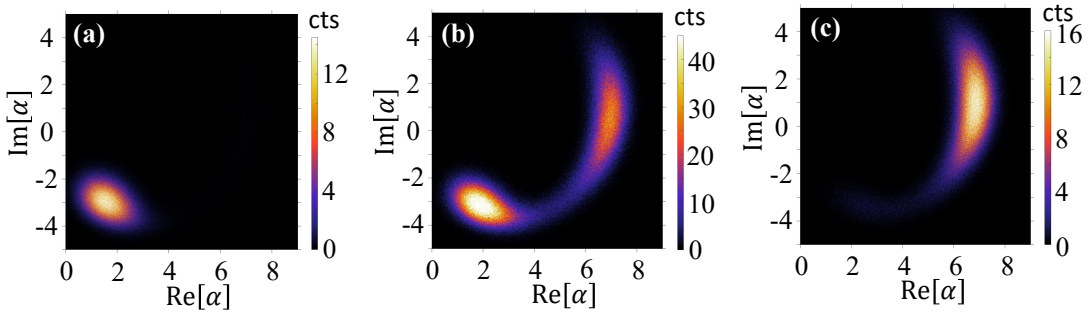

Figure 3.3: Quasiprobability distribution for the real and imaginary part of the cavity field for three values of the detuning. Brighter colors indicate a higher probability. Simulation parameters are the same as in Fig. 3.1.

Interestingly, the magnitude of the fluctuations is different in the two states. This is hard to notice in the time traces in Fig. 3.1, but is already more clearly visible when looking at the widths of the two Gaussians in Fig. 3.2. It becomes even more clear when we take a look at the (quasi)probability distribution of the intracavity field α in the complex plane, shown in Fig. 3.3. Here we can see two bright spots, corresponding to the two different density states. However, the spot corresponding to the high density state has a much wider spread in the imaginary part, indicating a larger variance of the fluctuations in this state, even though the variance of the noise that we put in stays the same.

The time spent in either of the two states between two switching events is known as the residence time[21], formally defined as follows. One can map the density $N(t)$ to a stochastic point process $\{t_i\}$ by setting a crossing threshold, N_0. Below this threshold the system resides in the low-density state, $N_\downarrow$, whereas above this threshold the system resides in the high-density state, $N_\uparrow$. The crossing threshold is determined by the local maximum in the double well potential, or equivalently, by the local minimum in the probability distribution of the photon number (Fig. 3.2(b)). The times $\{t_i\}$ are determined by the following procedure: acquisition starts at $t_0 = 0$ when the density first crosses the threshold N_0. Then, each subsequent time the threshold value is crossed, we observe another level crossing and record the corresponding time as t_i for the $(i+1)$-th crossing. One can then define the residence time between two subsequent events as $\tau(i) = t_i - t_{i-1}$. However, for our purpose it is useful to distinguish residence times in

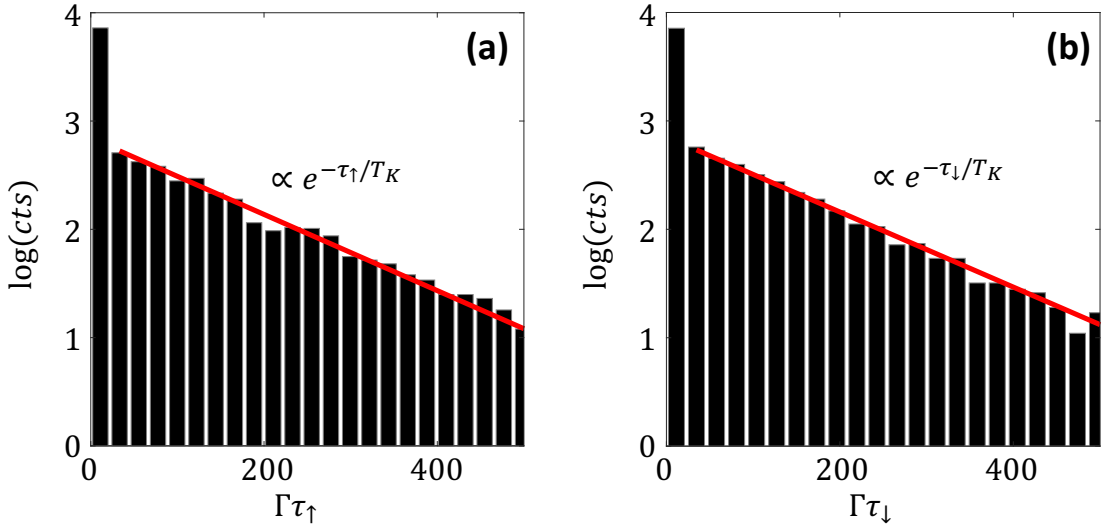

*Figure 3.4: Residence time distribution on a logarithmic scale for the high density state **(a)** and low density state **(b)**. From the fitted exponentials we obtain $T_K = 284\Gamma^{-1}$ and $T_{K,} = 289\Gamma^{-1}$ for the high and low density state, respectively. Simulation parameters are the same as in Fig. 3.1(b).*

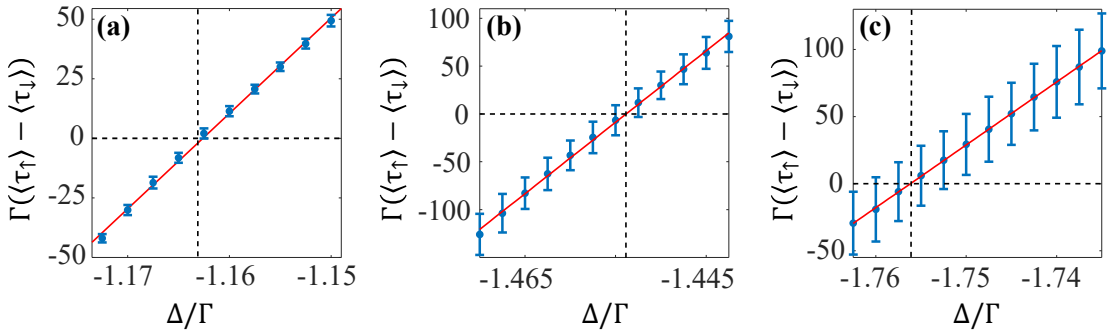

*Figure 3.5: Difference between the mean residence times of the high and low density state for $F = 5\Gamma$ **(a)**, $F = 6\Gamma$ **(b)** and $F = 7\Gamma$ **(c)**. Each point is the averaged result of 24 simulations with different seeds for the noise, where each simulation evolves the system from $t = 0$ to $t = 10^7\Gamma^{-1}$. Errorbars indicate one standard deviation of the mean. The red solid line is a linear fit to the data. The black dashed lines indicate where the fit is equal to zero, i.e. where the difference between the means is equal to zero, respectively at $\Delta/\Gamma = -1.1626$ **(a)**, $\Delta/\Gamma = -1.4538$ **(b)** and $\Delta/\Gamma = -1.7561$ **(c)**. Simulation parameters: $\Gamma = 1$, $\gamma = \Gamma/6$, $\kappa_1 = \Gamma/2$, $\kappa_2 = \Gamma/3$, $U = -\Gamma/40$, $D = 2\Gamma$.*

the high and low density states. This is done by considering in which state the system resides in the interval $\tau(i)$; if it is in the high density state, we set $\tau_\uparrow(i) = \tau(i)$, if it is in the low density state we set $\tau_\downarrow(i) = \tau(i)$. This way we can also use the residence times to determine how much time the system spends, on average, in either of the two states.

The residence time distributions (RTD) are shown in Fig. 3.4 for the same parameters as the trajectory in Fig. 3.1(b). The RTDs were computed by evolving the system for a long duration (from $t = 0$ to $t = 10^7\Gamma^{-1}$) and then following the above-described procedure. As expected from literature[21], we find exponential RTDs, i.e. the residence times τ are distributed according to $N(\tau) \propto \exp(-\tau/T_K)$, where T_K is a characteristic lifetime and gives us the Kramers escape rate $r_K = 1/T_K$[19;49]. As we will see in Chapter 4, this exponential behavior no longer holds when the interaction is non-instantaneous.

We observe a large deviation of the first bin from the exponential distribution and the origin is twofold. First off, there are some really fast consecutive crossings of the threshold we set, for which it is debatable whether or not they are actual switches between the two states or are due to numerical artifacts. The second reason is due to the finite bin duration: the first bin includes all events that are shorter than the bin duration. It thus also includes intrawell dynamics that cross the density threshold, and not only interwell dynamics.

Before we continue to the next section, it is useful to consider the average residence times $\langle\tau_{\uparrow,\downarrow}\rangle$, since this allows us to determine for which parameters the system spends an equal amount of time in either of the two states. This is done by evolving the system for a range of detunings in the bistable regime and computing the difference between the two average residence times, i.e. $\langle\tau_\uparrow\rangle - \langle\tau_\downarrow\rangle$, for each simulation. Assuming this difference depends linearly on the detuning when close to the center of the bistable regime, we fit a linear function to the data (Fig. 3.5) and use this to determine for which detuning $\langle\tau_\uparrow\rangle = \langle\tau_\downarrow\rangle$. This value is then used for the study of stochastic resonance in the next section.

3.2 Stochastic resonance

Now that we understand how the system behaves under the influence of Gaussian white noise, we are ready to study stochastic resonance. This not only requires a noisy environment, but also a subthreshold modulation of the detuning. Here, subthreshold means a modulation amplitude that does not induce level crossings in the absence of noise, i.e. we keep the modulation within the bistable regime. The idea behind stochastic resonance is to choose the right amount of noise, such that the average residence time is equal to half the modulation period[21].

In Fig. 3.6(a)-(d) we have shown the number of photons in the cavity as a function of time when modulating the detuning, for different values of the noise strength. The modulation of the detuning is chosen to be a triangular waveform, such that the speed of the scan in Δ is always

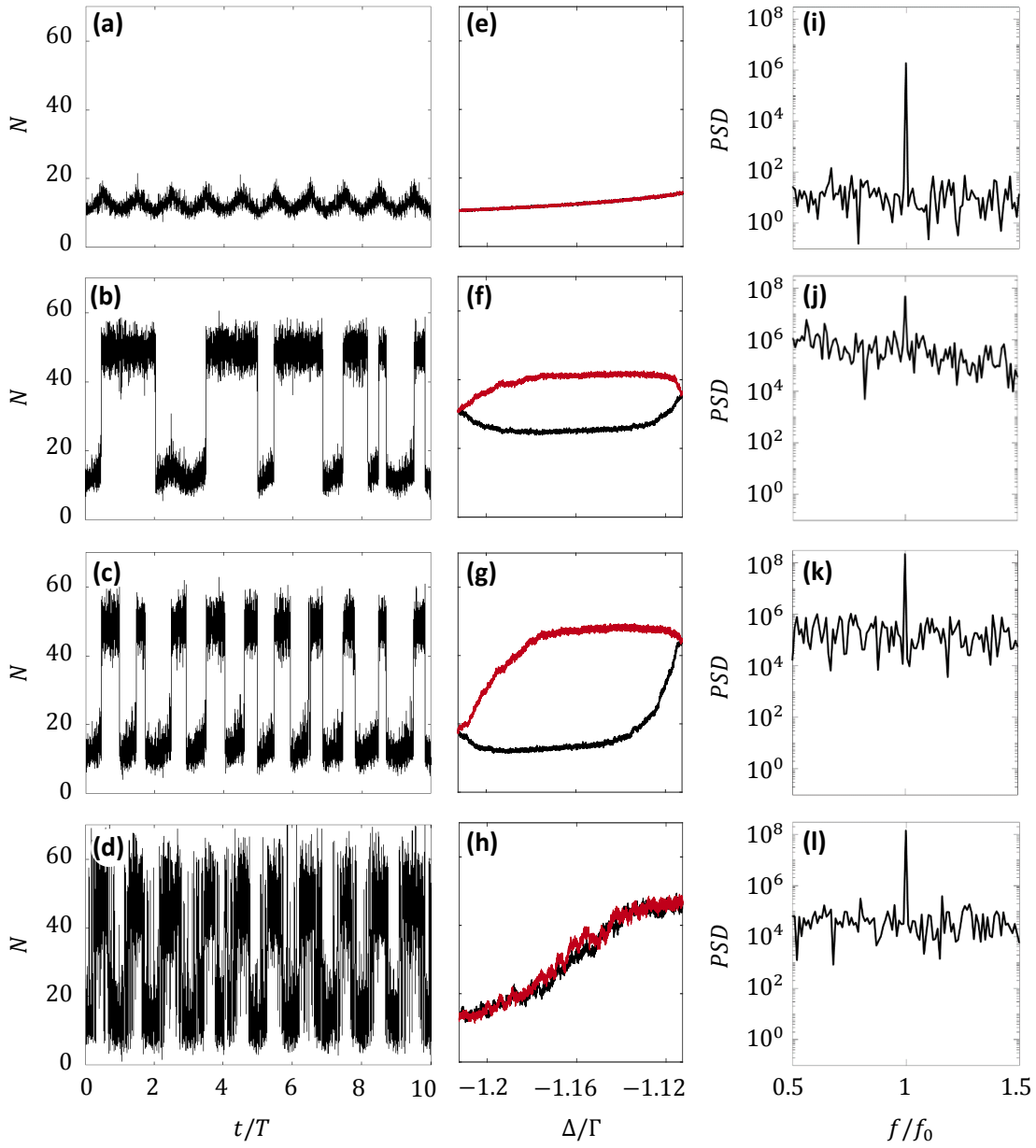

Figure 3.6: In ***(a)-(d)*** *we show simulations of the number of photons in the cavity when both noise and a periodic modulation of the detuning are present, for an increasing amount of noise (from top to bottom:* $D = 0.225\Gamma$, $D = 0.35\Gamma$, $D = 0.425\Gamma$ *and* $D = 0.8\Gamma$*). The mean and the extrema of the detuning modulation are the same values as used in Fig. 3.1. In* ***(e)-(h)*** *we show the corresponding positive (black) and negative trajectory (red) vs the detuning, averaged over* 100 *modulation periods. In* ***(i)-(l)*** *part of the corresponding power spectral density is shown. Simulation parameters:* $\Gamma = 1$, $\gamma = \Gamma/6$, $\kappa_1 = \Gamma/2$, $\kappa_2 = \Gamma/3$, $U = -\Gamma/40$, $F = 5\sqrt{\Gamma}$, $T = 10^4\Gamma^{-1}$, $\Delta_0 = -1.1626\Gamma$, $\Delta_{dif} = 0.1\Gamma$.

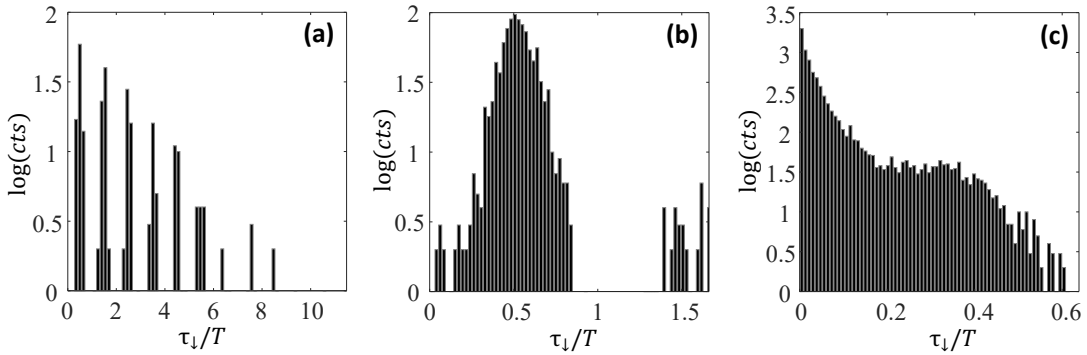

Figure 3.7: Residence time distributions of the low density state for three different noise levels when a small periodic modulation is present. The simulated noise strengths are ***(a)*** *$D = 0.35\Gamma$,* ***(b)*** *$D = 0.425\Gamma$ and (c) $D = 0.8\Gamma$, corresponding to Fig. 3.6(b)-(d), respectively. Simulation parameters are the same as in Fig. 3.6.*

constant, with the exception of the extrema in the waveform. We define these extrema as Δ_+ and Δ_- for the maxima and minima, respectively. The mean value of the modulation is then defined as $\Delta_0 = (\Delta_+ + \Delta_-)/2$ and the amplitude as $\Delta_{dif} = \Delta_+ - \Delta_-$. For later reference, we define the response of the system when the detuning is increased from Δ_- to Δ_+ as the positive trajectory, whereas the response when decreasing from Δ_+ to Δ_- is called the negative trajectory. In doing so, we are able to plot the average response of the system in both cases separately and study the differences.

When changing the noise strength while keeping all other parameters fixed, we can distinguish four different regimes, which are all shown in Fig. 3.6. The first regime, shown in (a), corresponds to a too low noise intensity to observe switching events in the first place. In this regime, the system will always stay either in the low or in the high density state, depending on its initial conditions. Therefore, the average of all positive trajectories is approximately the same as the average of all negative trajectories, as can be seen in Fig. 3.6(e).

In the second regime there is enough noise to observe level crossings, but these switching events are still random, as can be seen in Fig. 3.6(b). The reason for random switching events in this regime is that the noise intensity is still too low, such that the average residence time is less than half the modulation period. Therefore, we observe less than two level crossings per modulation period. However, since there are switching events, the average response of the system when increasing or decreasing the detuning is now different, such that we see a difference in the average positive and negative trajectories, as seen in (f). When looking at the residence time distribution in this regime (Fig. 3.7(a)), we observe a series of peaks, centered at odd multiples of half the modulation period T, i.e. at $(n - 1/2)T$, with n an integer, and the height of these peaks decays exponentially. The origin of these peaks is quite straightforwardly explained: The best time for the system to jump between the states is when the potential barrier is minimal, and this is exactly when the modulation is at one of its extrema. If the system switches at this point in time, then it takes another half period for the barrier to reach a minimum once more. Hence, $T/2$ is a preferred waiting time between level crossings. However, if the system doesn't jump between states when the potential barrier is minimal, it has to wait one full period before it reaches a minimum again. Therefore, the preferred residence intervals are odd multiples of the half modulation period. The exponential decay of the peak height is simply due to the already exponential decaying RTD in the absence of a modulation.

The third regime is when there is just the right amount of noise, such that the average residence time is equal to half the modulation period. This causes exactly two switching events per period, and from an energy perspective, it is most favorable to have these jumps occur at the modulation extrema. This synchronizes the level crossings with the modulation, known as stochastic resonance. The reasoning behind the name of this effect will become clear in a moment, when we will quantify this effect. Due to the increased coherence in the response of the system, we also see a more pronounced difference in the average positive and negative trajectories, shown in Fig. 3.6(g). This regime is furthermore characterized by a maximal area

under the peak at $T/2$ in the residence time distribution (Fig. 3.7(b)), also because the average residence time equals the half modulation period.

In the fourth and final regime there is too much noise present, such that the average residence time is shorter than half the modulation period, as seen in Fig. 3.6(d). This then leads to switching events in between half modulation periods, i.e. we observe more than two level crossings per period. The response of the system therefore becomes randomized and when increasing the noise strength more and more, the system will on average spend an equal amount of time in both states, during only half a modulation period. On average the positive and negative trajectories will therefore become equal again, as shown in (h). In the corresponding RTD in Fig. 3.7(c) this regime features a large amount of switching events a timescales shorter than $T/2$, as expected.

To quantify the effect of stochastic resonance, one has a multiple options, such as the signal-to-noise ratio (SNR) and the spectral amplification factor[21]. The SNR describes how well a signal is distinguishable from the background noise, and is defined as the ratio between the power in the delta-like peak in the power spectral density (PSD) at the modulation frequency (see Fig. 3.6(i)-(l) for reference) and the power of the noise, which can be computed as the mean in the PSD when excluding the peak at $f = f_0$. The resulting SNR as a function of the noise strength is shown in Fig. 3.8(a), showing a resonance-like peak. At first, the SNR decreases, which is true for any system when adding noise, but once the random switching events become synchronized with the modulation, the SNR quickly increases before decreasing again. This resonance-like behavior is where the term stochastic resonance originates from.

Another quantifier for stochastic resonance is based on the difference in the positive and negative trajectories. Specifically, we consider the area between the two average curves shown in Fig. 3.6(e)-(h), as function of the standard deviation of the noise. The result is shown in Fig. 3.8(b) and gives a very good indication for which noise strength the stochastic resonance takes place. At first, the area is zero, since the system doesn't switch between the two states. Then, as discussed previously, the level crossings starts to occur, causing a difference in the positive and negative trajectories, and therefore a nonzero area between the two average curves. The area reaches a maximum when there is a complete synchronization between the noise-induced switching events and the periodic driving. For a greater noise variance the area tends towards zero as the response of the system becomes random once more.

It is interesting to study how the stochastic resonance behavior depends on the different parameters of the system. In Fig. 3.6 we have shown the signal-to-noise ratio, SNR, and the hysteresis area, A, for three different modulation periods. This shows that when the modulation period is longer, the peak in both the SNR and in the area shift to lower noise strength. The reason is that the noise has more time to kick the system to the other state. In other words, since the (half) modulation period is longer, the mean residence time can also be longer, corresponding to a lower noise intensity.

In Fig. 3.9(a) we have shown the signal-to-noise ratio for three values of the driving strength F, with the respective mean detuning Δ_0 as found in Fig. 3.5. This shows that for an increased

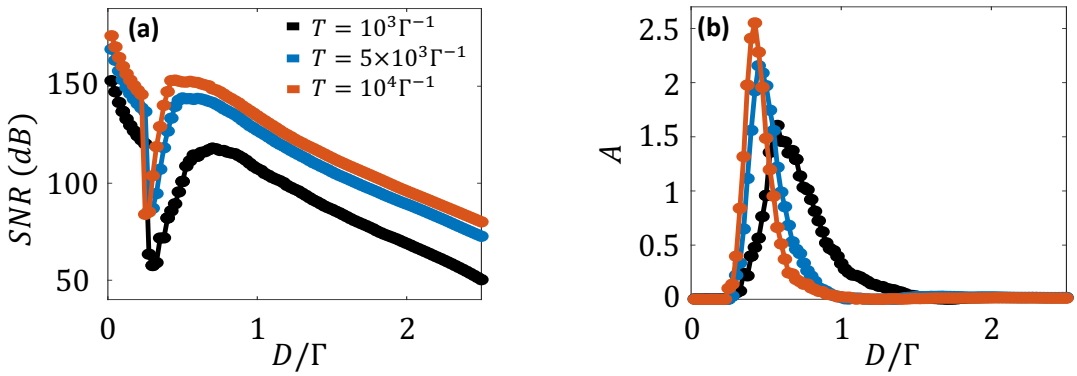

Figure 3.8: Signal-to-noise ratio ***(a)*** *and hysteresis area* ***(b)****, both as a function of the standard deviation of the noise and shown for three different values of the modulation period. Parameters:* $\Gamma = 1$, $\gamma = \Gamma/6$, $\kappa_1 = \Gamma/2$, $\kappa_2 = \Gamma/3$, $U = -\Gamma/40$, $F = 5\sqrt{\Gamma}$, $\Delta_0 = -1.1626\Gamma$, $\Delta_{dif} = 0.1\Gamma$.

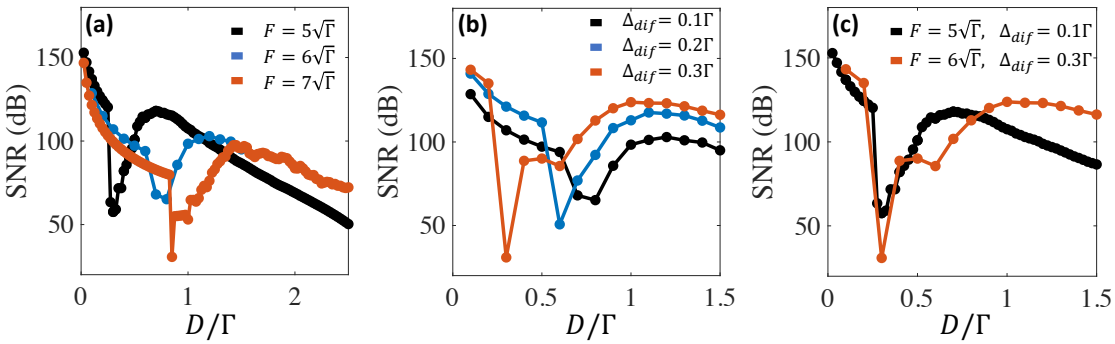

Figure 3.9: Signal-to-noise ratio as a function of standard deviation of the noise, shown for three driving amplitudes F in ***(a)*** *and for three modulation amplitudes Δ_{dif} at $F = 6\sqrt{\Gamma}$ in* ***(b)****. In* ***(c)*** *we show the combined effect of increasing the driving amplitude and the modulation amplitude. Parameters (unless stated otherwise): $\Gamma = 1$, $\gamma = \Gamma/6$, $\kappa_1 = \Gamma/2$, $\kappa_2 = \Gamma/3$, $U = -\Gamma/40$, $F = 5\sqrt{\Gamma}$, $\Delta_{dif} = 0.1\Gamma$, $T = 10^3\Gamma^{-1}$. Values of the modulation center Δ_0 are as computed in Fig. 3.5.*

driving strength, whilst keeping all other parameters fixed, the peak in the SNR shifts to a larger noise strength and the peak becomes smaller as well. This is because the barrier between the two states becomes larger when the driving strength increases, as can be seen in Fig. 3.10, where we show the calculated effective potential for various F. We thus require more noise to make the jump to the other state in the first place. However, by increasing the modulation amplitude Δ_{dif}, we can bring the system closer to the crossing threshold, such that less noise is required to make the jump. This results in an increased peak in the signal-to-noise ratio, which is shifted to smaller D (Fig. 3.9(b)), when all other parameters are kept fixed. Hence, when combining an increased driving strength with an increased modulation amplitude, one can reach an SNR comparable to a small driving strength with small modulation amplitude, as shown in Fig. 3.9(c).

To conclude this chapter, we provide a brief summary of the main points. First of all, we simulated a fixed nonlinear optical microcavity under the influence of noise and studied the residence time statistics. We found that the residence time distribution is exponentially decaying. By simulating the dynamics for a multitude of detuning values, we were able to determine the parameters for which the mean residence times in the high and low density state are equal. By then modulating the detuning around this value, we were able to study stochastic resonance by varying the amount of noise in the system. We saw that the right amount of noise synchronizes the switching events with the applied modulation. This leads to a resonance-like peak in the signal-to-noise ratio, which is known as stochastic resonance. Increasing the modulation period shifts the position of the peak in the SNR to lower noise strengths, because the system gets more time to make the jump to the other state. On the other hand, increasing the driving amplitude shifts the peak to higher noise intensities, because the barrier in the effective double

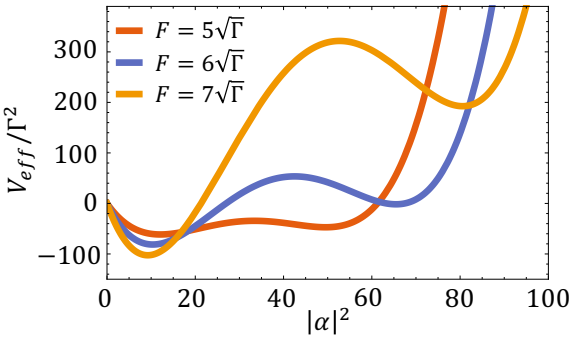

Figure 3.10: Effective potential for three values of the driving strength with the detuning as in Fig. 3.5, i.e. $\Delta = -1.1626\Gamma$ for $F = 5\sqrt{\Gamma}$, $\Delta = -1.4538\Gamma$ for $F = 6\sqrt{\Gamma}$, $\Delta = -1.7561\Gamma$ for $F = 7\sqrt{\Gamma}$. Parameters: $\Gamma = 1$, $\gamma = \Gamma/6$, $\kappa_1 = \Gamma/2$, $\kappa_2 = \Gamma/3$, $U = -\Gamma/40$.

well potential becomes larger and the system thus requires a stronger kick to cross.

Chapter 4

Non-Markovian stochastic resonance

Throughout the previous chapter we assumed an instantaneous effective photon-photon interaction. However, as discussed in Sec. 2.1, the nonlinearity of our system is based on a local temperature change in the medium inside the cavity. Since this temperature change is not instantaneous, the assumption of an instantaneous effective interaction does no longer hold. In this chapter we will discuss how we adjust the model to account for effective photon-photon interactions which are not instantaneous. As we will see, this introduces a memory effect in the interaction term in the equation of motion, making the system by definition non-Markovian. We will then study how this affects the residence time statistics of the system, before moving on to non-Markovian stochastic resonance.

4.1 Non-instantaneous interactions

Non-Markovian systems and generalized Langevin equations have been studied in detail during the second half of the previous century[50;51;52], also in the context of stochastic resonance[53;54]. The non-Markovian nature in these systems is due to non-instantaneous interactions between the system and the bath dissipating the energy lost by the system. These non-instantaneous system-bath interactions lead to correlated noise by the fluctuation-dissipation theorem[46], rendering the dynamics non-Markovian. The difference with the system we consider here is that the effective photon-photon interaction is not instantaneous, while the system-bath interactions are still assumed to be instantaneous.

To account for the non-instantaneous effective interaction, we take a similar approach as H. Mori in his 1965 paper[50]. However, where Mori introduces a memory kernel in the dissipative term in the equation of motion to account for colored noise, we put it in the interaction to account for the timescale of the effective photon-photon interactions. We will thus make the following substitution

$$U\left(|\alpha(t)|^2-1\right) \to \int_0^t \mathrm{d}s\; K(t-s)\left(|\alpha(s)|^2-1\right) \equiv w(t) \tag{4.1}$$

with the kernel function defined as

$$K(t) = \frac{U}{\tau}\mathrm{e}^{-t/\tau} \tag{4.2}$$

and characteristic timescale τ, which for a thermal nonlinearity would be the thermal relaxation time. The symbol should not be confused with the residence times $\tau_\uparrow$ and $\tau_\downarrow$ introduced in Sec. 3.1. However, the distinction will often be clear from context, or otherwise be stated explicitly.

It is important to note that with this definition of the memory kernel, the interaction strength can be written as

$$U = \int_0^\infty \mathrm{d}t\; K(t), \tag{4.3}$$

such that in the steady state, i.e. when $\alpha(t)$ is constant and can be taken out of the integral, we retrieve Eq. 3.1. This implies that the steady-state solutions are the same, regardless of having a memory kernel or not.

With this substitution we now have the integro-differential equation

$$\dot{\alpha}(t) = \left(i\Delta - \frac{\Gamma}{2} - iw(t)\right)\alpha(t) + \sqrt{\kappa_1}F, \tag{4.4}$$

which can be written as a set of two coupled ODEs by differentiating $w(t)$ with respect to t. This leads to

$$\begin{cases} \dot{\alpha}(t) = \left(i\Delta - \frac{\Gamma}{2} - iw(t)\right)\alpha(t) + \sqrt{\kappa_1}F \\ \dot{w}(t) = \tau^{-1}\left[U\left(|\alpha(t)|^2 - 1\right) - w(t)\right], \end{cases} \tag{4.5}$$

where, we used

$$\frac{d}{dx}\int_{a(x)}^{b(x)} \mathrm{d}t\, f(x,t) = f\left(x, b(x)\right) b'(x) - f\left(x, a(x)\right) a'(x) + \int_{a(x)}^{b(x)} \mathrm{d}t\, \frac{\partial f(x,t)}{\partial x}, \tag{4.6}$$

with the prime denoting a derivative with respect to x.

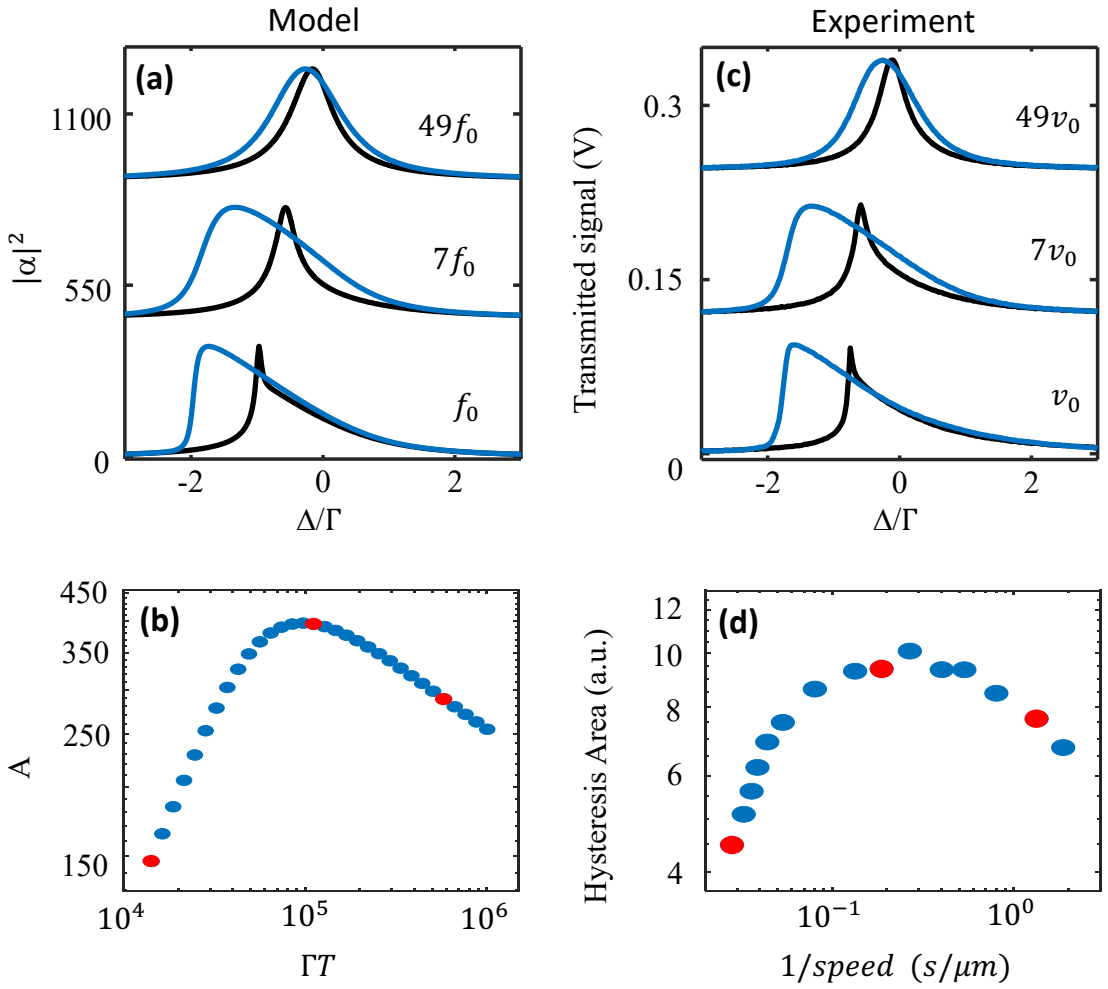

*Figure 4.1: Comparison of the dynamical hysteresis predictions of the model, **(a)** and **(b)**, and experimental results, **(c)** and **(d)**. Top panels show simulated (measured) dynamic hysteresis at three different scanning frequencies (speeds), corresponding to the red dots in the lower panels. The lower panels show the hysteresis area as a function of the period (1/speed). Measurements were performed by Zhou Geng.*

Having introduced the memory kernel $K(t)$ it should be obvious from Eq. 4.4 that the system is non-Markovian, since now the future states of the system explicitly depend on its past through the integration over $K(t)$. This introduces strong temporal correlations and as such makes the system inherently non-Markovian.

The effect of this non-instantaneous nonlinearity becomes very clear when we scan the detuning completely across the bistability (Fig. 4.1(a)). Simulations then show that the lineshape changes drastically when the period of the scan approaches the thermal relaxation time, τ. In fact, it becomes clear that as the period decreases and approaches the thermal relaxation time, the system appears to be not bistable anymore. This effect is in line with our reasoning that the effective interaction strength needs time to grow.

If we then look at how the hysteresis area changes as a function of the scanning period (Fig. 4.1(b)), we observe at first an increase in the area when we decrease the period, which is also true for an instantaneous nonlinearity [55]. However, we find there is a maximum in the area, after which it decreases again if we increase the speed of the scan even further. This closing of the area between the two trajectories is due to the insufficient nonlinearity at short timescales. As can also be seen, the predictions of the model agree very well with the experimental results (Fig. 4.1(c) and (d)).

4.2 Residence time analysis

Just as in the previous chapter, we start by studying how the system behaves under the influence of Gaussian white noise. To do so, we simulate the generalized Langevin equation we just derived, i.e.

$$\dot{\alpha}(t) = \left(i\Delta - \frac{\Gamma}{2} - i \int_0^t \mathrm{d}s \; K(t-s) \left(|\alpha(s)|^2 - 1 \right) \right) \alpha(t) + \sqrt{\kappa_1} F + D\zeta(t), \tag{4.7}$$

with $\zeta(t)$ the Gaussian white noise.

From our simulations it then becomes clear that to observe (a considerable amount of) level crossings within the same simulation time, we need to add a relatively large amount of noise. The amount of noise needed is so much that the variance of each of the two levels is larger than the distance between their means. This can be seen in the example trajectory in Fig. 4.2(a). Furthermore, as opposed to the Markovian simulations in Sec. 3.1, we no longer observe two Gaussian peaks in the probability distribution (Fig. 4.2(a)), but rather find one broad distribution. As a consequence, we can no longer use the same method to detect level crossings. We will now first discuss the method we use to detect the switching events based on statistics, before studying the residence time distributions.

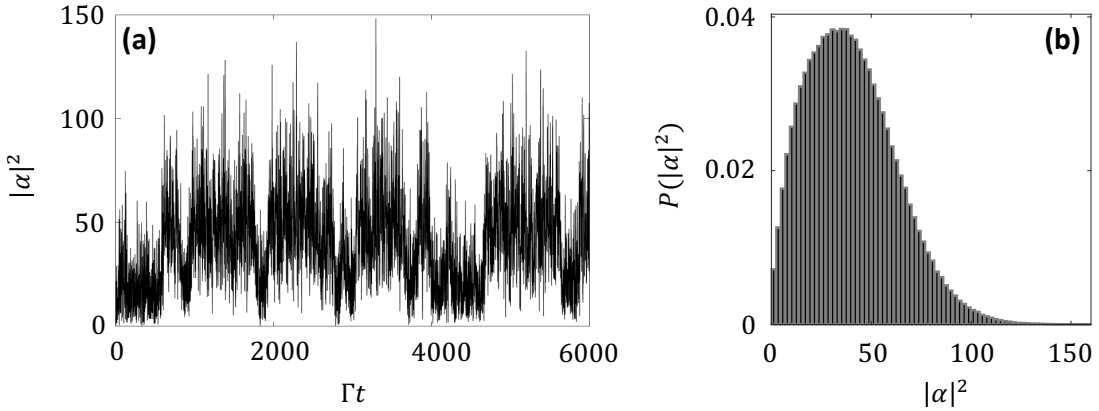

Figure 4.2: ***(a)*** *Simulation of the number of photons in the cavity for the model with a non-instantaneous interaction. In* ***(b)*** *the corresponding probability density is shown. Simulation parameters:* $\Gamma = 1$, $\gamma = \Gamma/6$, $\kappa_1 = \Gamma/2$, $\kappa_2 = \Gamma/3$, $\Delta = -1.21\Gamma$, $F = 5\sqrt{\Gamma}$, $U = -\Gamma/40$, $D = 2\Gamma$.

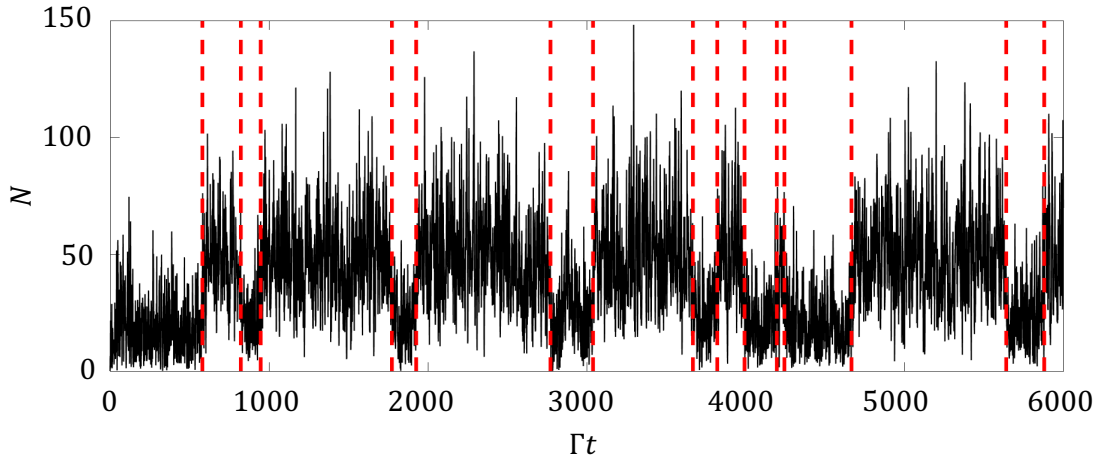

Figure 4.3: Simulation of the number of photons in the cavity for the model with a non-instantaneous interaction (black) and the detected change points in the mean (red). Simulation parameters are the same as in Fig. 4.2. The fixed penalty was set to be $\beta = 10^4$.

Change point detection

As the variance of each density level can now be larger than the difference between the means of each level, we need a different method to detect changes in the mean of the density. There are various methods available to detect these change points in a trajectory [56;57;58]. The method we will use is based on using penalized contrasts [59]. There is no particular reason for this choice other than that Matlab [48] has a built-in function (*findchangepts*) that uses this method to find the change points in a statistical property, e.g. the mean or variance, in a given trajectory.

The algorithm is as follows.

1. Choose a point and divide the signal in two subtrajectories at this point.
2. Compute the empirical estimate of the desired statistical property for each of the two subtrajectories.
3. For each data point within a subtrajectory, measure the deviation of the statistical property from the empirical estimate. Add the deviations of all points.
4. Add the deviations section-to-section to find the total residual error.
5. Vary the position of the division point until the total residual error reaches a minimum.
6. Repeat from 1 for the subsections before and after this division point.

Given a signal $x_1, x_2, ..., x_N$ containing K change points, it minimizes the cost function

$$J(K) = \sum_{r=0}^{K-1} \sum_{i=k_r}^{k_{r+1}-1} \delta\left(x_i; \chi\left(\left[x_{k_r} \dots x_{k_{r+1}-1}\right]\right)\right) + \beta K, \tag{4.8}$$

where $\chi\left(\left[x_{k_r} \dots x_{k_{r+1}-1}\right]\right)$ is the empirical estimate of the desired statistical property of the subtrajectory $x_{k_r} \dots x_{k_{r+1}-1}$, δ is the deviation measurement and β is a fixed penalty added for each change point to prevent overfitting.

Since we are interested in change points in the mean of a signal, μ, the function uses

$$\sum_{i=m}^{n} \delta(x_i; \chi([x_m \dots x_n])) = \sum_{i=m}^{n} (x_i - \mu([x_m \dots x_n]))^2 = (n-m+1)\mathrm{var}([x_m \dots x_n]). \tag{4.9}$$

By means of illustration, Fig. 4.3 shows an example trajectory and the changepoints detected by the above-described algorithm.

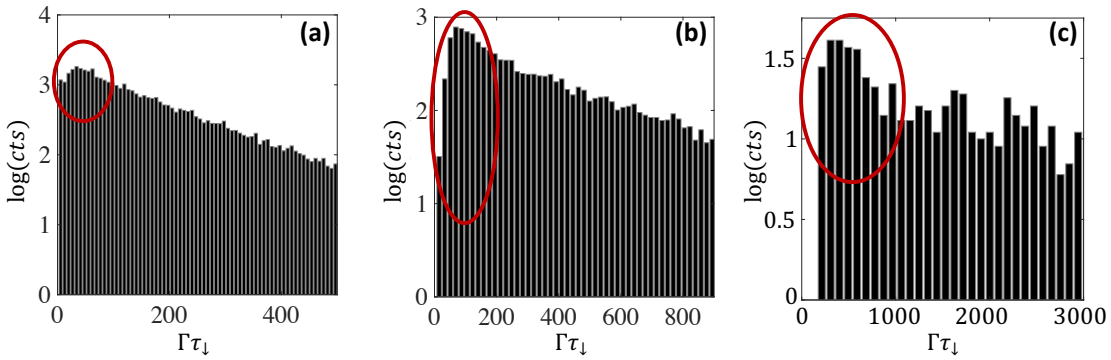

Figure 4.4: Residence time distributions of the low density state for three different values of the thermal relaxation time: ***(a)*** $\tau = 5\Gamma^{-1}$*,* ***(b)*** $\tau = 10\Gamma^{-1}$ *and* ***(c)*** $\tau = 25\Gamma^{-1}$*. Red circles indicate the deviation from an exponential distribution. The RTDs were formed by combining the residence time statistics of* 12 *separate simulations with different noise seeds. In each simulation the system was evolved from* $t = 0$ *to* $t = 10^7\Gamma^{-1}$*. Simulation parameters are the same as in Fig. 4.2. Penalties are set to be* $\beta = 5 \times 10^3$ *for* ***(a)****,* $\beta = 10^4$ *for* ***(b)*** *and* $\beta = 3 \times 10^4$ *for* ***(c)****.*

Effect of thermal relaxation on residence times

Now that we have a method to detect level crossings, we can compute the residence time distributions and see how these depend on the thermal relaxation time. We have done simulations for three values of the thermal relaxation time and the corresponding residence time distributions are shown in Fig. 4.4.

On timescales much longer than the thermal relaxation time the RTD retains its exponential behavior. This was to be expected, since on those timescales the effect of the memory kernel becomes negligible. Interestingly, however, on timescales comparable to the thermal relaxation time the shape deviates from the exponential one would get in the Markovian model. Deviating from the purely exponential behavior is a clear indication of non-Markovian dynamics[60], since it implies the level crossings are no longer independent of each other. Such RTDs have been observed experimentally in various systems[60;61;62], where stretched exponentials or power law behavior has been observed.

The fact that switching events on timescales shorter than the thermal relaxation time are suppressed are quite easily understood if one recalls that the thermal relaxation time sets the timescale for the effective interaction to grow. Essentially, this sets the reaction time of the system. On timescales shorter than the thermal relaxation time, the system doesn't react to small perturbations. Therefore, we don't observe level crossings on those timescales. On timescales comparable to the thermal relaxation time, the system is able to react. However, the level crossings are correlated, which is why the RTD deviates from a decaying exponential on these timescales. On time scales much larger than the thermal relaxation we observe the regular exponential decaying RTD, because the thermal relaxation time, and thus the correlation time of the level crossings, becomes negligible.

4.3 Stochastic resonance

To study stochastic resonance in this non-Markovian system, we again apply a weak periodic modulation to the detuning. Since the previous analysis of the residence times shows that level crossings on timescales comparable to the thermal relaxation time are heavily suppressed, we keep the modulation period considerably larger than the thermal relaxation time.

Fig. 4.5 shows the resulting signal-to-noise ratio (SNR) and hysteresis area as a function of the noise intensity. We have also shown the result with an instantaneous interaction for the same parameters as a reference in the same figure. This shows that in the non-Markovian model the general behavior under the influence of both noise and a periodic modulation is similar to when having an instantaneous interaction. We still observe the resonance-like peak in the SNR and in the hysteresis area, although the peak shifts to higher noise intensities when we increase

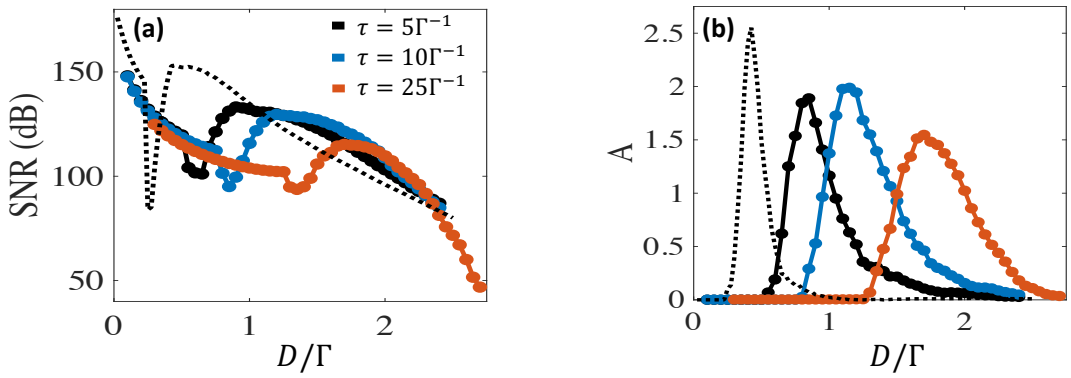

Figure 4.5: Signal-to-noise ratio ***(a)*** *and hysteresis area* ***(b)*** *as function of the standard deviation of the noise D, for different values of the thermal relaxation time. The black dashed line indicates the result of the model with instantaneous nonlinearity for the same parameters. Simulation parameters:* $\Gamma = 1$, $\gamma = \Gamma/6$, $\kappa_1 = \Gamma/2$, $\kappa_2 = \Gamma/3$, $F = 5\sqrt{\Gamma}$, $U = -\Gamma/40$, $\Delta_0 = -1.21\Gamma$, $\Delta_{dif} = 0.1\Gamma$, $T = 10^4\Gamma^{-1}$.

the thermal relaxation time. To understand this, we can follow the same line of reasoning as when we studied the residence time statistics. Because the nonlinearity of the system now needs time to grow, the system requires a stronger perturbation to make the jump to the other state. Since this time is defined by the thermal relaxation time, increasing the thermal relaxation time makes the reaction time of the system also longer, such that the strength of the perturbation required to cross the potential barrier becomes even larger. Hence, the noise intensity to obtain coherent level crossings shifts to larger values for a fixed modulation period.

A second observation we can make is a decrease in the height of the peak in the SNR, as well as a broadening of the peak. The reason for the decrease is the same as discussed in Sec. 3.2 when increasing the driving strength. The output power of the signal stays the same under the conditions of stochastic resonance, so the requirement of having more noise lowers the SNR. The broadening of the peak is due to the suppression of fast events, since it are mainly the fast events that lower the SNR after the peak, but these require a larger noise intensity to occur when the interaction is not instantaneous. In other words, the conditions for stochastic resonance become more robust to having too much noise. The same line of reasoning explains the decrease and broadening of the peak in the hysteresis area.

In systems with an instantaneous nonlinearity, stochastic resonance can be achieved by matching the mean residence time with the half modulation period. This can be done by either changing the noise intensity, which affects the escape rate, or by changing the modulation period itself. In this system with a non-instantaneous nonlinearity we obtain another means to reach the condition for stochastic resonance, which is by tuning the thermal relaxation time. In experiment, this would be done by changing the material inside the cavity.

Chapter 5

Observation of stochastic resonance

In this chapter we will discuss the experimental realization of stochastic resonance in an optical microcavity. First we shall address the experimental setup and the characterization of the system in Sec. 5.1. In Sec. 5.2 we discuss where we get the nonlinearity from and describe a method to determine the timescale of the nonlinearity. Finally, we cover the main results in Sec. 5.3, which show the experimental realization of stochastic resonance in an optical microcavity at room temperature.

5.1 Setup

The setup used to study stochastic resonance in a system with a non-instantaneous interaction consists of the following (see Fig. 5.1). The heart of our system is a tunable optical microcavity, consisting of one planar DBR mirror and one planar silver mirror with a thickness of $50nm$. At the center of the DBR mirror there is a square flat pillar of dimensions $200 \times 200\mu m^2$; we call it a plinth (shown in Fig. 5.2(a)). The small area of the plinth makes it easier to align the two mirrors parallel to each other. On top of the plinth there are micron-sized curved features milled out (Fig. 5.2(b)), such that the light can be contained in all three dimensions. The radius of curvature of these features ranges from 1.5 to 25μm and their depths from 200 to 600nm. For the main experiment, discussed in the next section, we used a microcavity with a 12μm radius of curvature and a 600nm depth.

The DBR mirror is situated on a piezo actuator with six degrees of freedom, such that we have full control over its position and orientation. This allows us to (i) align it with the silver mirror, (ii) select the curved feature we are interested in and (iii) set the initial distance between the two mirrors. The planar silver mirror is connected to a different piezo actuator, which can translate the mirror along one axis, allowing us to scan the cavity length. This change in cavity

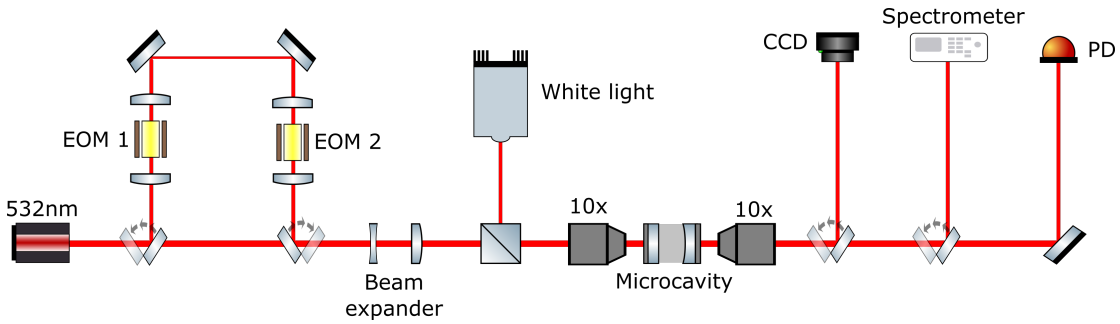

Figure 5.1: Schematic representation of the experimental setup. Both EOMs are connected to different waveform generators, such that we can use one to add noise to the amplitude of the laser and the other to add noise to the phase.

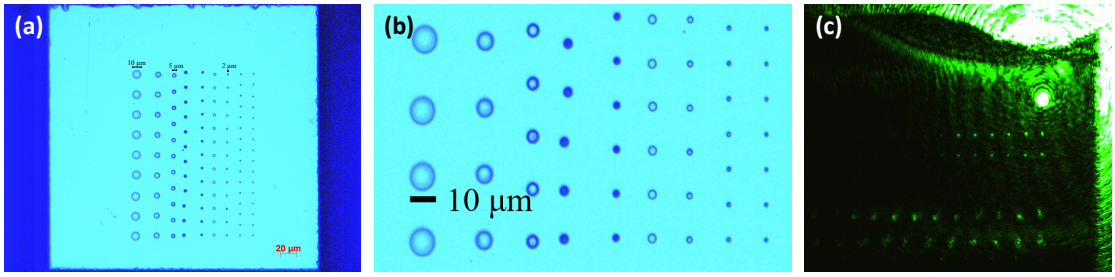

Figure 5.2: Optical microscope image of the plinth in ***(a)*** *with an enlargement of the curved micromirrors in* ***(b)****. In* ***(c)*** *we see the plinth in transmission when a 532nm laser is focused on the planar part. Resonances occur in some of the micromirrors due to a slight misalignment of the mirrors, such that some curved features are on resonance, whereas some are not.*

length changes the resonance frequency of the cavity. Thus, when the cavity is illuminated by a laser with constant frequency, we can control the detuning by changing the cavity length. In between the two mirrors we put a drop of macadamia oil, providing the thermal nonlinearity.

For the excitation we have two sources of light. One is a white light source, allowing simple imaging and white light transmission experiments. The other source is a single-mode 532nm laser, which is used for the main experiment. The laser light can be sent through two electro-optic modulators. These modulators are connected to different waveform generators, such that we can add noise to both the phase and the amplitude of the light. Using a 10x objective the light is then focused onto the sample, and then collected using another 10x objective. On the collection side of the cavity we have access to a CCD camera, a spectrometer and a photodiode. The photodiode is used for the main experiment discussed in the next section.

Focusing the white light source on a curved micromirror and using the spectrometer, we can take a white light transmission spectrum. Since we have control over the cavity length, we can take one spectrum, close the cavity one step (6nm due to software limitations) and take another spectrum. By repeating this process, we built the color map shown in Fig. 5.3, which shows the transmitted intensity as a function of both cavity length and wavelength. We observe enhanced transmission when the optical path length is an integer times half the wavelength, i.e. when the condition $nL = q\lambda/2$ is satisfied, with n the refractive index, L the cavity length, λ the wavelength and q the longitudinal mode number. Furthermore, for each longitudinal mode (the brightest and widest bands in Fig. 5.3) we observe a family of transverse modes (the narrower and less bright bands in Fig. 5.3). We did these measurements both for an empty cavity (Fig. 5.3(a)) and with macadamia oil inside (Fig. 5.3(b)), but other than a difference in contrast and a slight change in the distance between the modes, there is no striking difference between

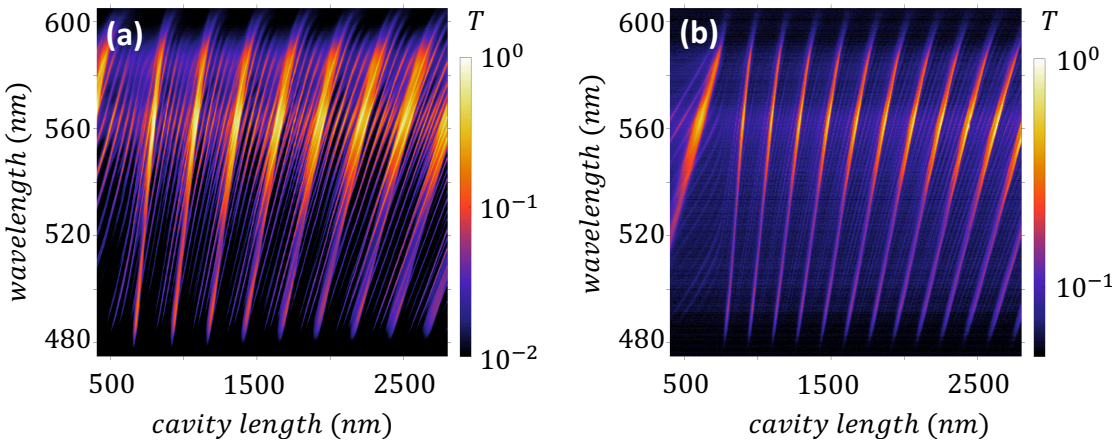

Figure 5.3: White light transmission spectrum as a function of cavity length, for an empty cavity ***(a)*** *and filled with macadamia oil* ***(b)****, when focusing the light on a micromirror with a* $12\mu m$ *radius of curvature and a* $600nm$ *depth.*

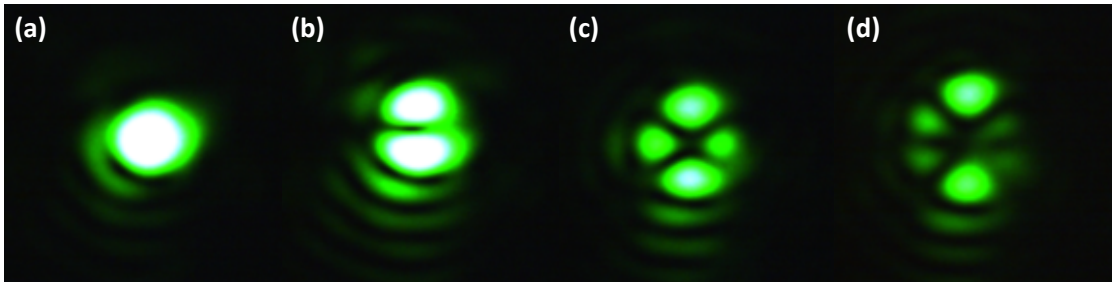

Figure 5.4: Transversal cavity modes in a cavity with a $12\mu m$ *radius of curvature and a depth of* $600nm$*. From* ***(a)-(d)*** *we can distinguish the zeroth up to the third order angular mode.*

the two. The difference in the distance between longitudinal modes is due to the difference in refractive index ($n = 1.4690$ for macadamia oil at $25°C$[63]).

To get back to the transversal cavity modes, we can visualize these by focusing the laser on a curved featured and then changing the cavity length until we hit one of those resonances. Using the camera we then observe the characteristic shapes of the transverse electromagnetic modes, shown in Fig. 5.4.

5.2 The nonlinear medium

The nonlinearity of the system is obtained by introducing macadamia oil in the cavity. As described in Sec. 2.1, a local temperature change of the medium, induced by the laser, causes a change in refractive index. This leads to nonlinear dynamics, because the refractive index now depends on the intensity of the incident light. As discussed in detail in Chapter 4, there is a characteristic timescale associated with the nonlinearity, because the local temperature change is not instantaneous. Here, we describe a method to extract this timescale from measurements.

From simulations (Fig. 5.5(b)) it follows that if we initialize the system at a driving strength on the left side of the bistability (see Fig. 2.1(c)) and then suddenly increase the driving strength to bring the system across the bistability, we observe an overshoot which has a full width at half maximum (FWHM) equal to half the thermal relaxation time, i.e. FWHM $= \tau/2$, (Fig. 2.1(e)). By sending the laser through the cavity and chopping the light at a relatively slow rate, we replicate this effect in the lab (Fig. 5.5(a)). This enables us to extract the thermal relaxation time from the FWHM of the overshoot. However, due to a lack of data points in the overshoot region, we are not comfortable to put an exact number to the thermal relaxation time yet. As a rough estimate, this method yields a thermal relaxation time of macadamia oil of $\sim 10\mu$s (Fig. 2.1(d)).

5.3 Experiments on non-Markovian stochastic resonance

To measure the stochastic resonance in our optical microcavity, we send the laser through the two modulators to add both phase and amplitude noise, similar to the simulations. We hereby note that due to scattering in the modulators, a lot of the initial laser power is lost. The measurements were performed using 20mW of laser power, which correspond to 2.2mW at the input of the cavity.

We furthermore need to modulate the detuning inside the bistable regime. This is done by starting out with a relatively large modulation amplitude and then decreasing it until we observe no more deterministic level crossings. This gives us a transmission signal as shown in part in Fig. 5.6(a). The modulation frequency was set at 50Hz, but as became clear from the Fourier transform (Fig. 5.6(e)), the actual frequency is slightly larger (53Hz).

By increasing the peak-to-peak voltage of the noise setting on the waveform generators, which directly determines the noise variance, we were able to observe random level crossings. Part of the measured trajectory is shown in Fig. 5.6(b). At this point it is important to note that we had to bias the system to the high density state, which is why the system stays in the high

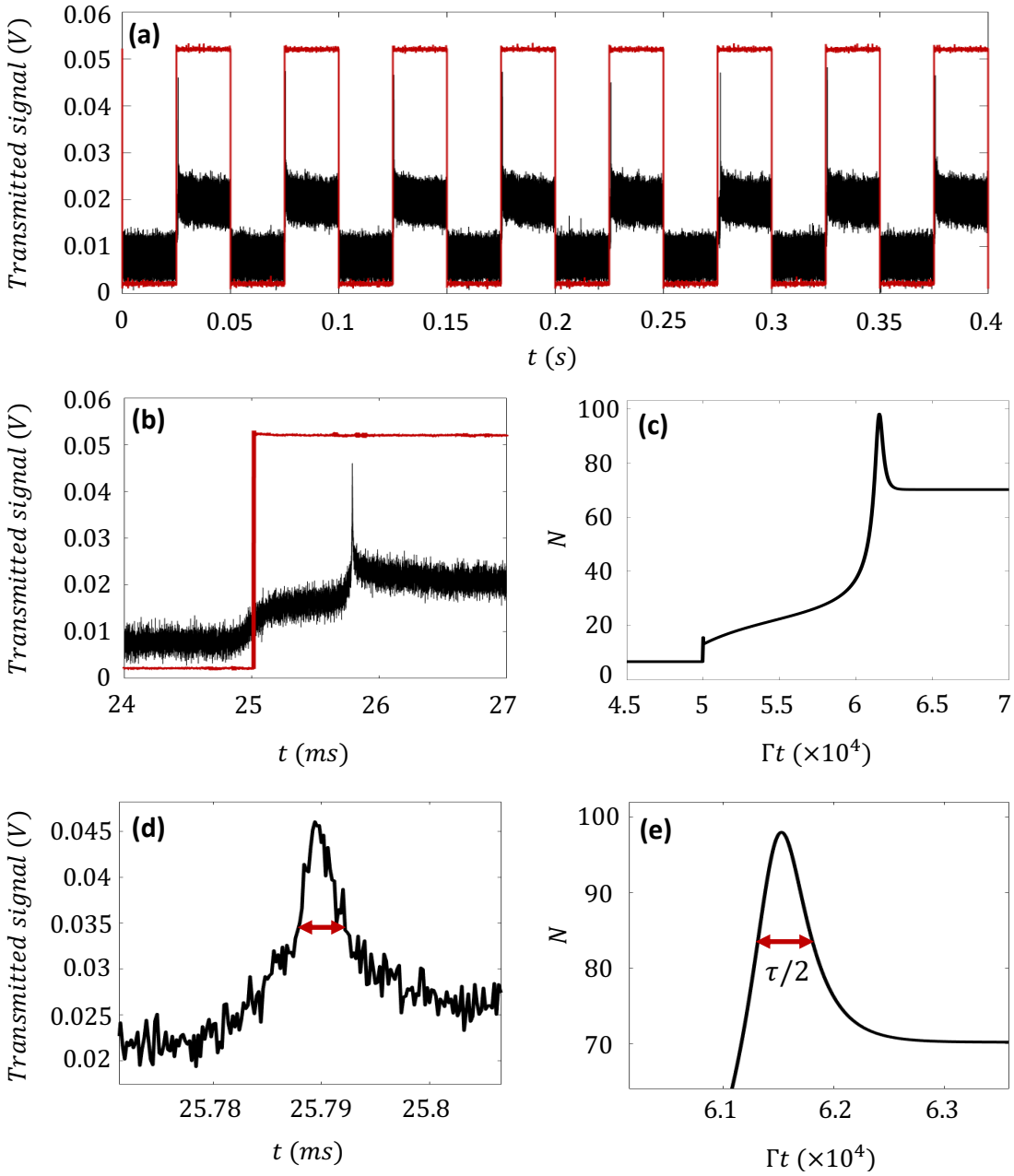

*Figure 5.5: Thermal relaxation measurement in **(a)** where the laser beam is chopped before entering the cavity. Red line displays the chopper signal, black is the transmission of the cavity. In **(b)** we show an enlarged section close to the level crossing, which shows comparable behavior as the simulation in **(c)**. In **(d)** and **(e)** we show enlargements of the overshoot, respectively for the measurement and the simulation, which have a full width at half maximum (red arrow) equal to the thermal relaxation time. Experimental parameters: Laser power 2mW, chopper frequency 20Hz, cavity ROC12 (depth 600nm), 8^{th} longitudinal cavity mode. Simulation parameters: $\Gamma = 1$, $\gamma = \Gamma/6$, $\kappa_1 = \Gamma/2$, $\kappa_2 = \Gamma/3$, $U = -\Gamma/40$, $\Delta = -\sqrt{2}\Gamma$, $F_{min} = 5\sqrt{\Gamma}$, $F_{max} = 7\sqrt{\Gamma}$, $\tau = 1000\Gamma^{-1}$.*

density state if it doesn't switch states. The reason we had to bias it, is due to a constant drift of the cavity length. The oil inside exerts a force on the mirrors, pushing them slowly apart. To counter this effect, we didn't set the cavity length in the center of the bistability, but slightly more closed, which corresponds to a less negative detuning and thus a bias of the high density state (see Fig. 3.1 for reference).

Increasing the peak-to-peak voltage even more, we get to the point where we observe coherent switching events (Fig. 5.6(c)). We notice that we needed a relatively large amount of noise,

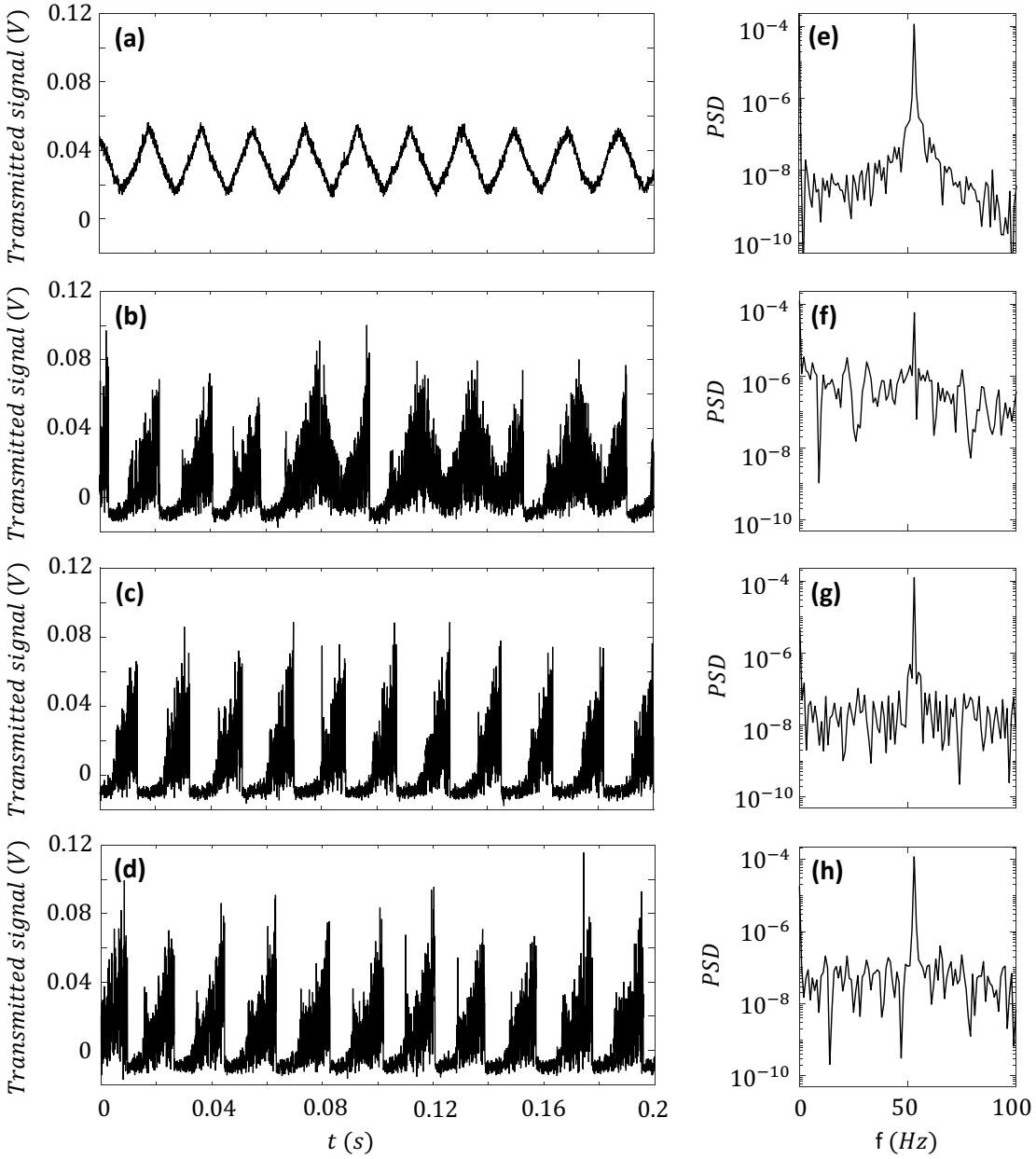

Figure 5.6: In ***(a)-(d)*** *we show sections of the measured transmitted signal when linearly modulating the cavity length at* $50Hz$ *over a distance of* $10nm$*, and under the influence of different noise intensities. In* ***(e)-(h)*** *we show the power spectral density in a frequency range close to the modulation frequency. The PSD is computed from the full signal, consisting of* ~ 50 *modulation periods. From top to bottom the peak-to-peak voltage set on the waveform generators is* $V_{PP} = 0$*,* $V_{PP} = 5$*,* $V_{PP} = 8$*,* $V_{PP} = 10$*. The measurements were performed using* $20mW$ *of laser power, corresponding to* $2.2mW$ *at the cavity input. The cavity we used has a radius of curvature of* $12\mu m$ *and a* $600nm$ *depth. In between the two mirrors was a drop of macadamia oil, acting as the thermal nonlinear medium.*

which we expected from the theory. Furthermore, we can clearly see that the variance of the high density state is much larger than of the low density state. This is likely to be due to vibrations in the cavity length, corresponding to noise in the detuning. This noise is multiplicative, as described in the introduction of Chapter 3, giving rise to the difference in variance of the two states.

Finally, we increase the peak-to-peak voltage to its maximum value, but this appeared to be not enough to observe multiple level crossings within a single half modulation period. Computing the signal-to-noise ratio as a function of the peak-to-peak voltage (Fig. 5.7(a)), we were therefore

not able to probe the stochastic resonance peak at high noise variances in the current state of our setup. However, we obtain a signal-to-noise ratio which shows the same behavior as found in the simulations (Fig. 5.7(b) for reference). At first, it decreases when increasing the amount of noise, and then at some point increases again. We do seem to have reached the maximum value of the peak in the SNR, but we did not observe the decay due to having reached the limit of our waveform generators and amplifiers.

From the measurements we can make the following conclusions. First and foremost, we observed signatures of stochastic resonance at room temperature in a system with a non-instantaneous nonlinearity, and the results are in line with our theoretical predictions. Secondly, in the current state of the setup there are two main issues to be solved. One is to change the amplifiers, such that a larger noise variance can be added to the incoming beam. This should then allow us to probe the full extent of the stochastic resonance peak in the signal-to-noise ratio. The second change to be made is to get rid of the constant drift in the cavity length. By implementing a feedback loop as described in the supporting information of Ref. 64, it should be possible to keep the mean position of the cavity fixed throughout the modulation. The method relies on sending two additional laser beams through the cavity and using the relative phase difference of their transmitted signal to build a feedback loop. According to the authors it should be possible to reach a positioning precision of around 10pm at a 50Hz refresh rate, in which they are limited by their software. This means that we can use this method and still apply a modulation, as long as the modulation frequency is much larger than the refresh rate.

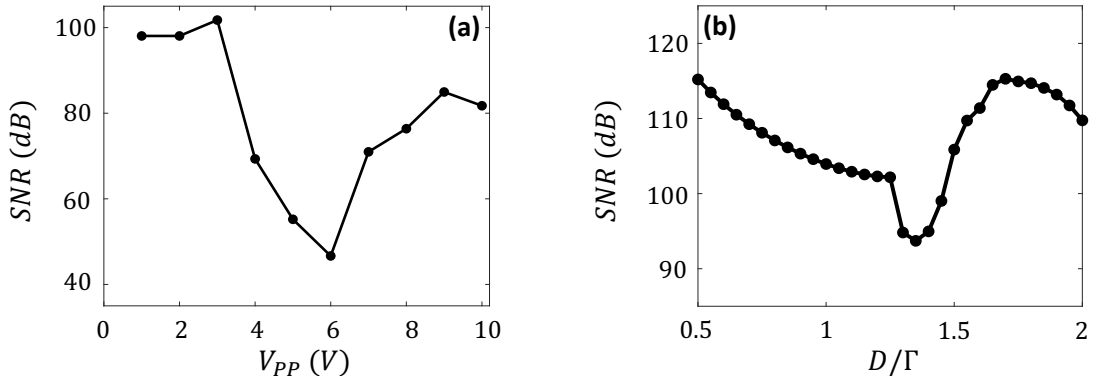

Figure 5.7: Measured signal-to-noise ratio as a function of the peak-to-peak voltage set on the waveform generators ***(a)****. In* ***(b)*** *we show the simulated result with* $\tau = 25\Gamma^{-1}$ *of Fig. 4.5 as a reference. Experimental parameters are the same as in Fig. 5.6.*

Chapter 6

Summary and Outlook

We conclude this thesis by providing a summary of the main theoretical and experimental results and an outlook to future research.

In Chapter 2 we introduced driven-dissipative nonlinear resonators. Here we discussed that a local change in temperature in the dispersive medium leads to a change in refractive index, which in turn leads to effective photon-photon interactions. These effective interactions make the system nonlinear, and cause it to become bistable under the right driving conditions. We derived the mean field equation of motion following the work by Drummond and Walls [34] and calculated the steady-state solutions to show the bistability.

We then built the foundation for the thesis in Chapter 3. We started out by discussing simulations of an optical microcavity with an instantaneous nonlinearity under the influence of noise. We found a bimodal probability distribution of the number of photons in the cavity and saw that we can bias the system in either of the two states by changing the detuning, which corresponds to a tilt of the effective double well potential. We then looked at the residence times in these two metastable states and found that their distributions are exponentially decaying, which is in agreement with the literature [21;49]. Next we applied a weak periodic modulation to the detuning and studied stochastic resonance by gradually increasing the amount of noise we put in the system. The results are once more in line with existing literature about stochastic resonance.

The main theoretical results were obtained in Chapter 4. Up to this point, an instantaneous nonlinearity was assumed. However, we know that the nonlinear term arises due to a local temperature change, which is not instantaneous. To account for this effect, we introduced a memory kernel in the effective interaction. We compared simulations where we scan the detuning completely across the bistability to experiments. This gives rise to dynamical hysteresis and we have shown that the predictions of the model agree nicely with the experimental results. We then study the residence times in this new model and find that their distributions are no longer exponential, a signature of a non-Markovian bistable system [60]. We concluded this chapter with simulations of the system under the influence of both noise and a weak periodic modulation and found again a peak in the signal-to-noise ratio as a function of the noise strength, indicating non-Markovian stochastic resonance. We found that the position of the resonance-like peak is determined by the characteristic timescale of the nonlinearity.

Finally, in Chapter 5, we discussed the experimental realization of stochastic resonance at room temperature in an optical microcavity with macadamia oil inside. We started out by giving an overview of the setup used for the experiment and discussed a method to measure the thermal relaxation time. Due to a limited temporal resolution we are not able to put a definitive number to the thermal relaxation time, but we roughly estimate a thermal relaxation time of macadamia oil of $\sim 10\mu$s. We then considered the results obtained when applying a weak periodic modulation to the cavity length and gradually increasing the amount of noise. The results clearly show a synchronization between the initially random switching events and the applied modulation. However, we were limited in the amount of noise we could apply and therefore we were only able to observe one side of the resonance-like peak in the signal-to-noise ratio.

The obtained experimental results are very promising. After some small changes to the

setup, we should be able to probe the full peak in the signal-to-noise ratio. The simplest change is to use different waveform generators and amplifiers, such that we can apply more noise to the system. The other improvement that needs to be made is to stabilize the cavity against the constant drift, which is due to the force exerted on the mirrors by the oil in between them. We are currently working on implementing the method described in the supplementary material of Ref. 64.

Now that we understand the properties of a single nonlinear microcavity under the influence of noise, we want to continue our line of research to coupled cavities. First we will analyze two coupled cavities to study multistability and spontaneous symmetry breaking [65], particularly how the latter is affected by having a non-instantaneous nonlinearity. Ultimately we envisage nonlinear cavities on a lattice, such that we can study (noise assisted) transport in complex networks [16] and possible topological effects. Having access to such lattices furthermore allows us to construct an analog simulator for the Ising model, as it has been shown that a lattice of bistable optical resonators can be mapped to the Ising model [66].

Bibliography

[1] A. Einstein. Über die von der molekularkinetischen Theorie der Wärme geforderte Bewegung von in ruhenden Flüssigkeiten suspendierten Teilchen. *Annalen der Physik*, 322(8):549–560, 1905.

[2] A. Einstein. Zur Theorie der Brownschen Bewegung. *Annalen der Physik*, 324(2):371–381, 1906.

[3] P. Langevin. Sur la théorie du mouvement brownien. *Comptes rendus de l'Académie des sciences*, 146:530–533, 1908.

[4] J.B. Johnson. Thermal agitation of electricity in conductors. *Physical Review*, 32(1):97–109, June 1928.

[5] H. Nyquist. Thermal agitation of electric charge in conductors. *Physical Review*, 32(1):110–113, July 1928.

[6] John K. Douglass, Lon Wilkens, Eleni Pantazelou, and Frank Moss. Noise enhancement of information transfer in crayfish mechanoreceptors by stochastic resonance. *Nature*, 365(6444):337–340, September 1993.

[7] David F. Russell, Lon A. Wilkens, and Frank Moss. Use of behavioural stochastic resonance by paddle fish for feeding. *Nature*, 402(6759):291–294, November 1999.

[8] W. Hohmann, J. Müller, and F. W. Schneider. Stochastic resonance in chemistry. 3. the minimal-bromate reaction. *The Journal of Physical Chemistry*, 100(13):5388–5392, 1996.

[9] D.V. Dylov and J.W. Fleischer. Nonlinear self-filtering of noisy images via dynamical stochastic resonance. *Nature Photonics*, 4:323–328, 2010.

[10] R. de J. León-Montiel and Juan P. Torres. Highly efficient noise-assisted energy transport in classical oscillator systems. *Phys. Rev. Lett.*, 110:218101, May 2013.

[11] André Longtin, Adi Bulsara, and Frank Moss. Time-interval sequences in bistable systems and the noise-induced transmission of information by sensory neurons. *Physical Review Letters*, 67(5):656–659, July 1991.

[12] F. Caruso, A. W. Chin, A. Datta, S. F. Huelga, and M. B. Plenio. Highly efficient energy excitation transfer in light-harvesting complexes: The fundamental role of noise-assisted transport. *The Journal of Chemical Physics*, 131(10):105106, 2009.

[13] Patrick Rebentrost, Masoud Mohseni, Ivan Kassal, Seth Lloyd, and Alán Aspuru-Guzik. Environment-assisted quantum transport. *New Journal of Physics*, 11(3):033003, March 2009.

[14] Ivan Kassal and Alán Aspuru-Guzik. Environment-assisted quantum transport in ordered systems. *New Journal of Physics*, 14(5):053041, May 2012.

[15] Silvia Viciani, Manuela Lima, Marco Bellini, and Filippo Caruso. Observation of noise-assisted transport in an all-optical cavity-based network. *Phys. Rev. Lett.*, 115:083601, August 2015.

[16] Filippo Caruso, Nicolò Spagnolo, Chiara Vitelli, Fabio Sciarrino, and Martin B. Plenio. Simulation of noise-assisted transport via optical cavity networks. *Phys. Rev. A*, 83:013811, January 2011.

[17] Ido Dayan, Moshe Gitterman, and George H. Weiss. Stochastic resonance in transient dynamics. *Physical Review A*, 46(2):757–761, July 1992.

[18] Rosario N. Mantegna and Bernardo Spagnolo. Noise enhanced stability in an unstable system. *Physical Review Letters*, 76(4):563–566, January 1996.

[19] H.A.Kramers. Brownian motion in a field of force and the diffusion model of chemical reactions. *Physica*, 7(4):284–304, April 1940.

[20] C. Schmitt, B. Dybiec, P. Hänggi, and C. Bechinger. Stochastic resonance vs. resonant activation. *Europhysics Letters*, 74(6), 2006.

[21] Luca Gaimmaitoni, Peter Hänggi, Peter Jung, and Fabio Marchesoni. Stochastic resonance. *Review of Modern Physics*, 70(1), January 1998.

[22] Charles R. Doering and Jonathan C. Gadoua. Resonant activation over a fluctuating barrier. *Physical Review Letters*, 69(16):2318–2321, October 1992.

[23] Philip Pechukas and Peter Hänggi. Rates of activated processes with fluctuating barriers. *Physical Review Letters*, 73(20):2772–2775, November 1994.

[24] R. Benzi, A. Sutera, and A. Vulpiani. The mechanism of stochastic resonance. *Journal of Physics A*, 14(11):L453–L457, November 1981.

[25] C. Nicolis and G. Nicolis. Stochastic aspects of climatic transitions-additive fluctuations. *Tellus*, 33(3):225–234, June 1981.

[26] Roberto Benzi, Giorgio Parisi, Alfonso Sutera, and Angelo Vulpiani. A theory of stochastic resonance in climatic change. *SIAM Journal of Applied Mathematics*, 43(3):565–578, July 1983.

[27] Bruce McNamara, Kurt Wiesenfeld, and Rajarshi Roy. Observation of stochastic resonance in a ring laser. *Physical Review Letters*, 60(25):2626–2629, June 1988.

[28] E. C. Gage and L. Mandel. Investigation of dye-ring-laser statistics with controlled asymmetry. *Physical Review A*, 38(10):5166–5173, November 1988.

[29] L. Mandel, Rajarshi Roy, and Surendra Singh. Optical bistability effects in a dye ring laser. In *Optical Bistability*, pages 127–150, Boston, MA, 1981. Springer US.

[30] H. Abbaspour, S. Trebaol, F. Morier-Genoud, M. T. Portella-Oberli, and B. Deveaud. Stochastic resonance in collective exciton-polariton excitations inside a gaas microcavity. *Physical Review Letters*, 113(5):057401, July 2014.

[31] A. Baas, J. Ph. Karr, H. Eleuch, and E. Giacobino. Optical bistability in semiconductor microcavities. *Physical Review A*, 69(2):023809, February 2004.

[32] H. Abbaspour, S. Trebaol, F. Morier-Genoud, M. T. Portella-Oberli, and B. Deveaud. Spinor stochastic resonance. *Physical Review B*, 91(15):155307, April 2015.

[33] Timo Wagner, Peter Talkner, Johannes C. Bayer, Eddy P. Rugeramigabo, Peter Hänggi, and Rolf J. Haug. Quantum stochastic resonance in an a.c.-driven single-electron quantum dot. *Nature*, 15(4):330–334, February 2019.

[34] P.D. Drummond and D.F. Walls. Quantum theory of optical bistability I: Nonlinear polarisability model. *Journal of Physics A: Mathematical and General*, 13, 1980.

[35] J.P. Gordon, R.C.C. Leite, R.S. Moore, S.P.S. Porto, and J.R. Whinnery. Long transient effects in lasers with inserted liquid samples. *Journal of Applied Physics*, 1136(1):033003, May 1965.

[36] S.J. Sheldon, L.V. Knight, and J.M. Thorne. Laser-induced thermal lens effect: a new theoretical model. *Applied Optics*, 21(9), May 1982.

[37] Robert W. Boyd. *Nonlinear Optics*. Elsevier, 2003.

[38] N. Bloembergen. *Nonlinear optics*. New York: W.A. Benjamin, 1965.

[39] S.R.K. Rodriguez, V. Goblot, N. Carlon Zambon, A. Amo, and J. Bloch. Non-reciprocity and zero reflection in nonlinear cavities with tailored loss. *Physical Review A*, 99(1), January 2019.

[40] G. Kordas, D. Witthaut, P. Buonsante, A. Vezzani, R. Burioni, A.I. Karanikas, and S. Wimberger. The dissipative Bose-Hubbard model: Methods and examples. *The European Physical Journal Special Topics*, 224:2127, September 2015.

[41] Carlos Navarrete-Benlloch. Open systems dynamics: simulating master equations in the computer, arXiv:1504.05266, April 2015.

[42] S.R.K. Rodriguez, W. Casteels, F. Storme, N. Carlon Zambon, I. Sagnes, L. Le Gratiet, E. Galopin, A. Lemaître, A. Amo, C. Ciuti, and J. Bloch. Probing a dissipative phase transition via dynamical optical hysteresis. *Physical Review Letters*, 118(247402), June 2017.

[43] Haibin Wu, Surendra Singh, and Min Xiao. Multiplicative noise-induced probability distributions in three-level atomic optical bistability. *Physical Review A*, 79(2):023835, February 2009.

[44] Daniel T. Gillespie. The mathematics of brownian motion and johnson noise. *American Journal of Physics*, 63(3), August 1995.

[45] Li Zhang, Li Cao, and Da jin Wu. Effect of correlated noises in an optical bistable system. *Physical Review A*, 77(1):015801, January 2008.

[46] R. Kubo. The fluctuation-dissipation theorem. *Reports on Progress in Physics*, 29(1):255, 1966.

[47] S. Kiesewetter, R. Polkinghorne, B. Opanchuk, and P. D. Drummond. *SowftwareX*, March 2016.

[48] MATLAB. *version 9.5.0 (R2018b)*. The MathWorks Inc., Natick, Massachusetts, 2018.

[49] Peter Hänggi, Peter Talkner, and Michal Borkovec. Reaction-rate theory: fifty years after kramers. *Review of Modern Physics*, 62(2):251–341, April 1990.

[50] H. Mori. Transport, collective motion and Brownian motion. *Progress of Theoretical Physics*, 33(3):423, March 1965.

[51] P. Hänggi. Correlation functions and masterequations of generalized (non-Markovian) Langevin equations, June 1978.

[52] Peter Hänggi and Fatemeh Mojtabai. Thermally activated escape rate in presence of long-time memory. *Physical Review A*, 26(2):1168, February 1982.

[53] Igor Goychuk and Peter Hänggi. Non-markovian stochastic resonance. *Physical Review Letters*, 91(7):070601, August 2003.

[54] Igor Goychuk and Peter Hänggi. Theory of non-markovian stochastic resonance. *Physical Review E*, 69(2):021104, February 2004.

[55] W. Casteels, F. Storme, A. Le Boité, and C. Ciuti. Power laws in the dynamic hysteresis of quantum nonlinear photonic resonators. *Physical Review A*, 93(3):033824, March 2016.

[56] Jaxk Reeves and Jien Chen. A review and comparison of changepoint detection techniques for climate data. *Journal of applied meteorology and climatology*, 46(6):900, June 2007.

[57] S. Aminikhanghahi and D.J. Cook. A survey of methods for time series change point detection. *Knowledge and information systems*, 52(2):339, June 2017.

[58] Charles Truong, Laurent Oudre, and Nicolas Vayatis. Selective review of offline change point detection methods, arxiv:1801.00718, January 2019.

[59] Marc Lavielle. A survey of methods for time series change point detection. *Signal processing*, 85:1501, October 2004.

[60] M. Boguna, A.M. Berezhkovskii, and G. H. Weiss. Residence time densities for non-markovian systems. (I). the two-state system. *Physica A*, 282:475–485, July 2000.

[61] L.S.Liebovitch and J.M.Sullivan. Fractal analysis of a voltage-dependent potassium channel from cultured mouse hippocampal neurons. *Biophysical Journal*, 52(6):979–988, December 1987.

[62] Szymon Mercik and Karina Weron. Stochastic origins of the long-range correlations of ionic current fluctuations in membrane channels. *Physical Review E*, 63(5):051910, April 2001.

[63] ROSHILA MOODLEY, ANDREW KINDNESS, and SREEKANTH B. JONNALAGADDA. Elemental composition and chemical characteristics of five edible nuts (almond, brazil, pecan, macadamia and walnut) consumed in southern africa. *Journal of Environmental Science and Health Part B*, 42(5):585 – 591, June 2007.

[64] A. A. P. Trichet, P. R. Dolan, D. James, G. M. Hughes, C. Vallance, and J. M. Smith. Nanoparticle trapping and characterization using open microcavities. *NANO letters*, 16(10):6172–6177, September 2016.

[65] Davide Sarchi, Iacopo Carusotto, Michiel Wouters, and Vincenzo Savona. Coherent dynamics and parametric instabilities of microcavity polaritons in double-well systems. *Physical Review B*, 77(12):125324, March 2008.

[66] M. Foss-Feig, P. Niroula, J. T. Young, M. Hafezi, A. V. Gorshkov, R. M. Wilson, and M. F. Maghrebi. Emergent equilibrium in many-body optical bistability. *Physical Review A*, 95(4):043826, April 2017.

Appendix A

Mean field cavity EOM

Here we will derive the equation of motion for the cavity field in the mean field approximation, i.e. Eq. 2.11. For the mean field approximation, we assume the field is coherent with amplitude $\alpha(t) = \langle \hat{a} \rangle$. We also note that the expectation value of an operator $\hat{A}$ is given by $\langle \hat{A} \rangle = \mathrm{Tr}(\hat{A}\hat{\rho})$. We thus have

$$\dot{\alpha} = \frac{d}{dt}\langle a \rangle = \frac{d}{dt}\mathrm{Tr}\left(\hat{a}\hat{\rho}\right) = \mathrm{Tr}\left(\hat{a}\frac{d\hat{\rho}}{dt}\right), \tag{A.1}$$

where for the last step we used the fact that we are working in the Schrödinger picture, meaning operators are time-independent.

Next, we insert the master equation (Eq. 2.10), such that we get the following two terms on the right-hand side

$$\dot{\alpha} = \; i\,\mathrm{Tr}\left(\hat{a}[\hat{\rho}, \hat{H}(t)]\right) + \frac{\Gamma}{2}\mathrm{Tr}\left(2\hat{a}\hat{a}\hat{\rho}\hat{a}^\dagger - \hat{a}\hat{a}^\dagger\hat{a}\hat{\rho} - \hat{a}\hat{\rho}\hat{a}^\dagger\hat{a}\right). \tag{A.2}$$

Starting with the first term on the right, we insert the Hamiltonian (Eq. 2.8), leading to the following three terms

$$\begin{aligned} i\,\mathrm{Tr}\left(\hat{a}[\hat{\rho}, \hat{H}(t)]\right) &= i\omega_0 \mathrm{Tr}\left(\hat{a}[\hat{\rho},\, \hat{a}^\dagger\hat{a}]\right) && \text{(A.3a)} \\ &\quad + i\frac{U}{2}\mathrm{Tr}\left(\hat{a}[\hat{\rho},\, \hat{n}(\hat{n}-1)]\right) && \text{(A.3b)} \\ &\quad - \sqrt{\kappa_1}\mathrm{Tr}\left(\hat{a}[\hat{\rho},\, F\mathrm{e}^{-i\omega t}\hat{a}^\dagger + F^*\mathrm{e}^{i\omega t}\hat{a}]\right) && \text{(A.3c)} \end{aligned}$$

From here, we will repeatedly use the trace's property of cyclic invariance, i.e. $\mathrm{Tr}(\hat{a}\hat{b}\hat{c}) = \mathrm{Tr}(\hat{b}\hat{c}\hat{a}) = \mathrm{Tr}(\hat{c}\hat{a}\hat{b})$, to write all traces in the form $\mathrm{Tr}[f(\hat{a}, \hat{a}^\dagger)\hat{\rho}] = \langle f(\hat{a}, \hat{a}^\dagger)\rangle$. We will show the process for A.3a explicitly, the other terms follow from the same procedure. We have

$$\begin{aligned} i\omega_0 \mathrm{Tr}\left(\hat{a}[\hat{\rho},\, \hat{a}^\dagger\hat{a}]\right) &= i\omega_0 \mathrm{Tr}\left(\hat{a}\hat{\rho}\hat{a}^\dagger\hat{a} - \hat{a}\hat{a}^\dagger\hat{a}\hat{\rho}\right) \\ &= i\omega_0\left(\left\langle \hat{a}^\dagger\hat{a}\hat{a}\right\rangle - \left\langle \hat{a}\hat{a}^\dagger\hat{a}\right\rangle\right) \\ &= i\omega_0\left(\left\langle (\hat{a}\hat{a}^\dagger - 1)\hat{a}\right\rangle - \left\langle \hat{a}\hat{a}^\dagger\hat{a}\right\rangle\right) \\ &= -i\omega_0\alpha. \end{aligned} \tag{A.4}$$

Here we made use of the commutation relation $[\hat{a}_j, \hat{a}_k^\dagger] = \delta_{jk}$ to get from the second line to the third.

Similarly using the cyclic property of the trace and the commutator for the creation and annihilation operators, we find for A.3b and A.3c

$$i\frac{U}{2}\mathrm{Tr}\left(\hat{a}[\hat{\rho},\, \hat{n}(\hat{n}-1)]\right) = -iU\alpha\left(|\alpha|^2 - 1\right) \tag{A.5}$$

and

$$-\sqrt{\kappa_1}\mathrm{Tr}\left(\hat{a}[\hat{\rho},\, F\mathrm{e}^{-i\omega t}\hat{a}^\dagger + F^*\mathrm{e}^{i\omega t}\hat{a}]\right) = \sqrt{\kappa_1}F\mathrm{e}^{-i\omega t} \tag{A.6}$$

For the term involving U, we furthermore used a semiclassical approximation, such that correlation functions factorize.

We now have

$$i\,\mathrm{Tr}\left(\hat{a}[\hat{\rho},\hat{H}(t)]\right) = -i\left[\omega_0 + U\left(|\alpha|^2 - 1\right)\right]\alpha + \sqrt{\kappa_1}F\mathrm{e}^{-i\omega t} \tag{A.7}$$

and in a similar fashion one can easily show that the second term in Eq. A.2 can be written as

$$\frac{\Gamma}{2}\mathrm{Tr}\left(2\hat{a}\hat{a}\hat{\rho}\hat{a}^\dagger - \hat{a}\hat{a}^\dagger\hat{a}\hat{\rho} - \hat{a}\hat{\rho}\hat{a}^\dagger\hat{a}\right) = -\frac{\Gamma}{2}\alpha. \tag{A.8}$$

Finally, inserting A.7 and A.8 in A.2 leads to

$$i\dot{\alpha} = \left[\omega_0 - i\frac{\Gamma}{2} + U\left(|\alpha|^2 - 1\right)\right]\alpha + i\sqrt{\kappa_1}F\mathrm{e}^{-i\omega t}, \tag{A.9}$$

which is the equation of motion for the field inside the cavity in the mean field approximation.

Appendix B

Bogoliubov-like excitations

Here we will derive Eq. 2.16, which describes the evolution of fluctuations in the field in the microcavity.

Using Eq. 2.12 and its complex conjugate, we can write

$$i\frac{\partial}{\partial t}\begin{pmatrix}\alpha\\-\alpha^*\end{pmatrix}=\begin{pmatrix}\left[-\Delta-i\frac{\Gamma}{2}+U\left(|\alpha|^2-1\right)\right]\alpha+i\sqrt{\kappa_1}F\\\left[-\Delta+i\frac{\Gamma}{2}+U\left(|\alpha|^2-1\right)\right]\alpha^*-i\sqrt{\kappa_1}F^*\end{pmatrix}. \tag{B.1}$$

Then by substituting $\alpha\to\alpha+\delta\alpha$, with $\delta\alpha$ a small deviation from the steady-state solution α, we obtain

$$i\frac{\partial}{\partial t}\begin{pmatrix}\alpha+\delta\alpha\\-\alpha^*-\delta\alpha^*\end{pmatrix}=\begin{pmatrix}\left[-\Delta-i\frac{\Gamma}{2}+U\left(|\alpha+\delta\alpha|^2-1\right)\right](\alpha+\delta\alpha)+i\sqrt{\kappa_1}F\\\left[-\Delta+i\frac{\Gamma}{2}+U\left(|\alpha+\delta\alpha|^2-1\right)\right](\alpha^*+\delta\alpha^*)-i\sqrt{\kappa_1}F^*\end{pmatrix}.$$

Since we assume the fluctuations are small, we only need to consider the lowest order terms in $\delta\alpha$. Neglecting higher order terms leads to

$$i\frac{\partial}{\partial t}\begin{pmatrix}\alpha+\delta\alpha\\-\alpha^*-\delta\alpha\end{pmatrix}=\begin{pmatrix}\left[-\Delta-i\frac{\Gamma}{2}+U\left(|\alpha|^2-1\right)\right](\alpha+\delta\alpha)+U\left(\alpha^2\delta\alpha^*+|\alpha|^2\delta\alpha\right)+i\sqrt{\kappa_1}F\\\left[-\Delta+i\frac{\Gamma}{2}+U\left(|\alpha|^2-1\right)\right](\alpha^*+\delta\alpha^*)+U\left(|\alpha|^2\delta\alpha^*+(\alpha^*)^2\delta\alpha\right)-i\sqrt{\kappa_1}F^*\end{pmatrix}.$$

Now note that for the steady-state solution the following condition holds

$$0=i\frac{\partial}{\partial t}\begin{pmatrix}\alpha\\-\alpha^*\end{pmatrix}=\begin{pmatrix}\left[-\Delta-i\frac{\Gamma}{2}+U\left(|\alpha|^2-1\right)\right]\alpha+i\sqrt{\kappa_1}F\\\left[-\Delta+i\frac{\Gamma}{2}+U\left(|\alpha|^2-1\right)\right]\alpha^*-i\sqrt{\kappa_1}F^*\end{pmatrix},$$

such that we get

$$i\frac{\partial}{\partial t}\begin{pmatrix}\delta\alpha\\-\delta\alpha^*\end{pmatrix}=\begin{pmatrix}\left[-\Delta-i\frac{\Gamma}{2}+U\left(|\alpha|^2-1\right)\right]\delta\alpha+U\left(\alpha^2\delta\alpha^*+|\alpha|^2\delta\alpha\right)\\\left[-\Delta+i\frac{\Gamma}{2}+U\left(|\alpha|^2-1\right)\right]\delta\alpha^*+U\left(|\alpha|^2\delta\alpha^*+(\alpha^*)^2\delta\alpha\right)\end{pmatrix}.$$

This can finally be rewritten as

$$i\frac{\partial}{\partial t}\begin{pmatrix}\delta\alpha\\\delta\alpha^*\end{pmatrix}=\begin{pmatrix}-\Delta-i\frac{\Gamma}{2}+U\left(2|\alpha|^2-1\right) & U\alpha^2\\-U(\alpha^*)^2 & \Delta-i\frac{\Gamma}{2}-U\left(2|\alpha|^2-1\right)\end{pmatrix}\begin{pmatrix}\delta\alpha\\\delta\alpha^*\end{pmatrix}, \tag{B.2}$$

which we identify with Eq. 2.16.